

Multiscale perspective on wetting on switchable substrates: mapping between microscopic and mesoscopic models

Moritz Stieneker,^{1,2} Leon Topp,^{3,*} Svetlana Gurevich,^{1,2,†} and Andreas Heuer^{3,2,4,‡}

¹*Institute for Theoretical Physics, University of Münster,
Wilhelm-Klemm-Str. 9, 48149 Münster, Germany*

²*Center of Nonlinear Science (CeNoS), University of Münster, Corrensstr. 2, 48149 Münster, Germany*

³*Institute for Physical Chemistry, University of Münster,
Correnstr. 28/30, 48149 Münster, Germany*

⁴*Center for Multiscale Theory and Computation (CMTC),
University of Münster, Corrensstr. 40, 48149 Münster, Germany*

(Dated: April 8, 2024)

To understand the non-equilibrium relaxation dynamics of a liquid droplet on a switchable substrate the interplay of different length- and time-scales needs to be understood. We present a method to map the microscopic information, resulting from a molecular dynamics simulation, to a mesoscopic scale, reflected by a thin film model. After a discussion of the mapping procedure we first analyze the relaxation of a liquid droplet upon switching the wettability of the substrate. Further, we show that a nearly identical mapping procedure can be used for the description of two coalescing droplets. With our procedure we take a first step to extend the mapping from the equilibrium case to non-equilibrium wetting dynamics, thus allowing for a quantitative multi-scale analysis.

I. INTRODUCTION

Finding ways to manipulate and control patterns of liquids has been the goal of scientists for a long time. Back in 1992 Chaudhury and Whitesides were able to exploit a wettability gradient to make a droplet walk up an incline [1]. Another example includes extensively experimental studies of the instabilities, dynamics, and morphological transitions of patterns in thin liquid films on

* M. Stieneker and L. Topp contributed equally to this work.

† gurevics@uni-muenster.de

‡ andheuer@uni-muenster.de

different pre-structured substrates, see e.g., [2–6]. Nowadays such systems can also be examined theoretically on different length- and timescales [7–12], e. g. transversal instabilities of ridges on pre-structured substrates have been studied with a combination of a microscopic kinetic Monte Carlo model and a continuous thin film model [13–15].

In recent years the development of switchable surfaces gained pace. On such surfaces the wettability can be varied by applying an external stimulus like changing the pH value or by illumination with light of a defined wavelength. Prominent examples for such surfaces are inorganic materials like TiO_2 or ZnO [16–18] which have the advantage of a large difference between the contact angles before and after switching. Since the switching process from the hydrophilic to the hydrophobic case for these substrates is rather slow, another class of substrates is of great interest, namely substrates coated with a self-assembled monolayer (SAM) consisting of molecules with azobenzene or other photoresponsive moieties [19–21]. The azobenzene moiety can be switched with UV light from a trans to a cis state which has a lower wettability while the reverse process can be induced by illumination with blue light. These surfaces adapt much faster at the disadvantage of lower contact angle differences. However, in recent years improvements which yield a higher change of the contact angle have been made by microstructuring the surface [22, 23].

Switchable substrates promise rich non-equilibrium behavior and an additional mechanism to control pattern formation, which can be employed in addition to static pre-structures. In particular it was demonstrated that it is possible to guide the movement of a droplet in a reversible manner by applying a light gradient [21, 24], i. e. changing the wettability close to the droplet. Recent theoretical work by Grawitter and Stark [25] investigated how droplets can be steered with the help of spatio-temporal wettability patterns using the macroscopic boundary element method. This is relevant especially for the development of lab-on-a-chip devices [26].

Theoretical models play a key role to gain an improved understanding of the non-equilibrium behavior on switchable substrates. In particular, to study microscopic phenomena, atomistic simulation methods like Molecular Dynamics (MD) have become an established approach [27–29]. On larger length- and time-scales, mesoscopic thin film descriptions have been successfully applied for a variety of different wetting systems, see the reviews [30–32]. While the microscopic MD simulations can incorporate more details of the specific interactions between liquid and substrate, continuum mesoscopic models cannot resolve microscopic details but are able to address much larger length and time scales. Furthermore, continuous mesoscopic models allow to apply the tool kit of bifurcation analysis to investigate instabilities offering analytical insights which is not

possible in discrete, microscopic models. Bifurcation analysis combined with parameter sweeps, which are computationally cheaper compared to microscopic models, can then indicate interesting parameter regimes and time scales to analyze in the microscopic model for a more detailed investigation. This helps avoiding computational costs for simulations in irrelevant regimes.

Thus, combining different microscopic and continuous descriptions seems natural and has been done by Wu *et al.* [14], among others. There, spreading dynamics of drops on solid surfaces was investigated by solving the Navier–Stokes equations in a continuum domain comprised of the main body of the drop together with MD simulations in a particle domain in the vicinity of the contact line. Another example for the combination of models across length- and timescales is the work by Zhang *et al.* who combined MD with volume of fluid simulations to study droplet spreading on surfaces [15]. Also Hadjiconstantinou supplied both, a continuum and MD method for the flow of two immiscible fluids in a channel [33]. In [13], kinetic Monte Carlo simulations and a thin-film continuum model were combined to comparatively study the Plateau-Rayleigh instability of ridges formed on pre-structures substrates. It was shown that the evolution of the occurring instability qualitatively agrees between the two models.

Given the advantages and disadvantages of the different methods, it is evident that a mapping between the methods is of great interest. For the static case various microscopic descriptions have been employed to improve the mesoscopic models mainly by extracting the binding potential (also referred to as the wetting, disjoining or interface potential) [34, 35]. For partially wetting liquids, the interface potential is particularly important for describing the droplets in the vicinity of the three-phase contact line. It is defined for a uniform thickness layer of the liquid on a flat solid wall in the presence of a bulk vapor phase.

In particular, Tretyakov *et al.* extracted properties from a MD model to study equilibrium properties in a continuum model and found quantitative agreements between the MD model and the continuum model [36]. Similar results can be obtained based on density-functional theory [35, 37]. The results obtained in [35, 37] could be verified by a different method of extracting the disjoining pressure, namely using nudged elastic band calculations[38]. Hughes *et al.* could relate oscillatory disjoining pressures to layering effects and found qualitative agreements to profile shapes observed in experiments [35].

However, so far the focus has been on static equilibrium conditions. As switchable substrates inherently lead to non-equilibrium dynamics, static considerations are not sufficient anymore. Therefore, our focus here is on the mapping of the time scales.

In this paper we propose a general method to map a MD model to a mesoscopic thin film model making the first step towards quantitative comparisons of dynamics between mesoscopic and microscopic models. We illustrate the method by analyzing the switching behavior on a homogeneous substrate and the coalescence of two ridges. Our mapping procedure for the parameters responsible for the substrate wettability can be applied on its own for static comparisons between both models.

The functional form of the presented mapping can help to understand differences between the employed models and shed light into the corresponding time scales and transport quantities. A mapping between the model parameters can possibly provide insights, if continuum models are able to grasp all the features present in particle-based, microscopic models.

II. THEORETICAL BACKGROUND

A. Molecular Dynamics theory

On the microscopic level, we employ the framework HOOMD [39] to perform simulations of a system consisting of Lennard-Jones particles in the canonical ensemble. All particles in the system are interacting through the Lennard-Jones potential

$$V(r_{lj}) = 4\epsilon_{lj} \left(\left(\frac{\sigma_{lj}}{r_{lj}} \right)^{12} - \left(\frac{\sigma_{lj}}{r_{lj}} \right)^6 \right), \quad (1)$$

where r_{lj} is the distance of particles l and j , ϵ_{lj} the interaction strength between the particles and $\sigma_{lj} = \frac{1}{2}(\sigma_l + \sigma_j)$ the mean of the particles' diameters σ_l and σ_j . This potential is truncated and shifted at a cut-off radius of $r_c = 2.5\sigma$. The interaction strength is calculated as the geometric mean of the self interaction parameters $\epsilon_{lj} = \sqrt{\epsilon_l \epsilon_j}$. We distinguish two types of particles, namely the substrate particles (here denoted with "s"), which are fixed at their positions during the simulation, and the fluid ones (denoted with "l") which form the droplet or are in the gas phase. While the interaction strength of the droplet particles is set to $\epsilon_l = 1$ for all simulations, by varying the parameter ϵ_s the wettability of the surface can be changed. Note that $\epsilon_w = \sqrt{\epsilon_s \epsilon_l} = \sqrt{\epsilon_s}$ denotes the interaction strength between a liquid and substrate particle, because we set $\epsilon_l = 1$. In all simulations we vary the value ϵ_w between $\epsilon_{HW} = 0.762$ for a high wettability and $\epsilon_{LW} = 0.632$ for a low wettability if not denoted otherwise. The particle diameter is set to $\sigma_l = \sigma_s = \sigma$ for the solid as well as for the fluid particles. The time step is set to $\tau = \sigma^{-1} \sqrt{\epsilon/M}/200$, where M is

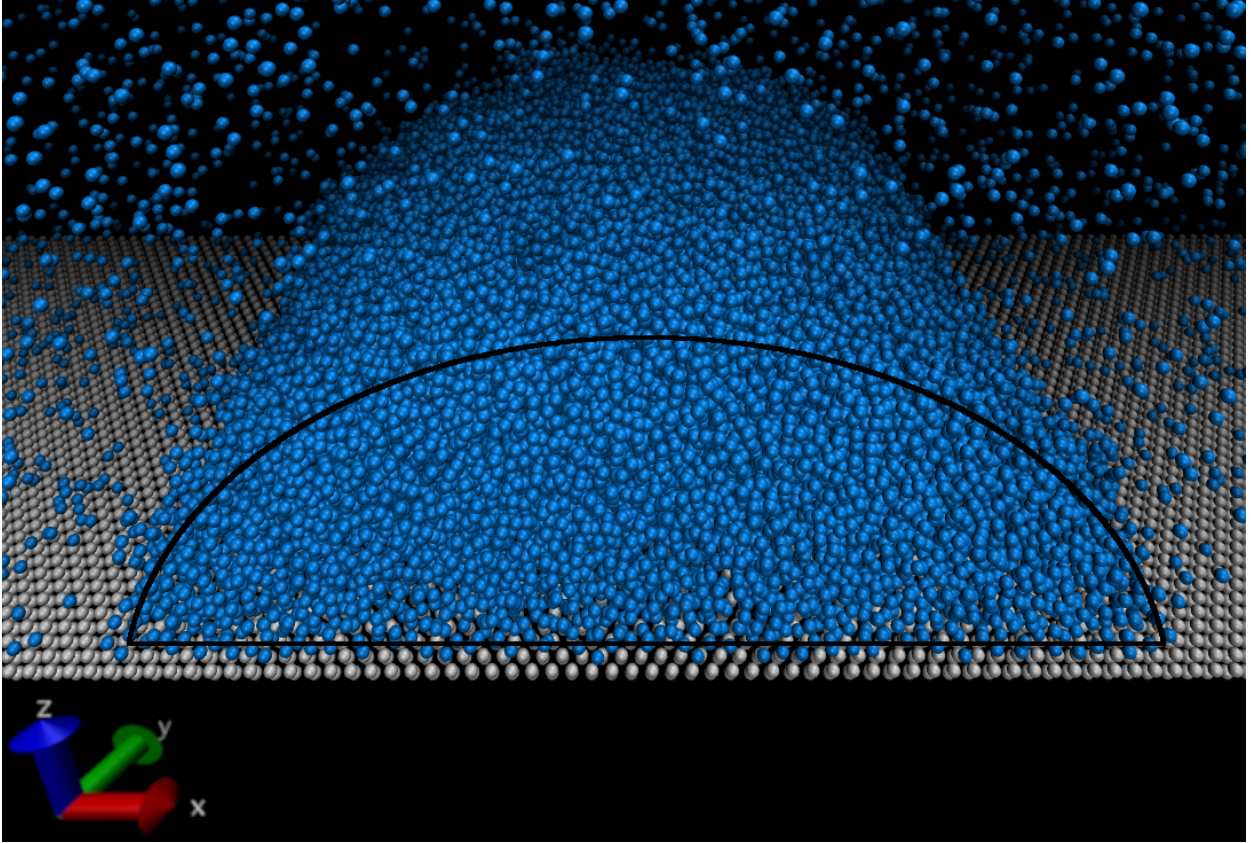


FIG. 1: Snapshot from a MD simulation showing droplet particles (blue) forming a cylindrically shaped droplet placed on two layers of a fcc(111) surface.

the particle mass and the reduced temperature is $\frac{k_B T}{\epsilon} = 0.75$. The substrate particles are arrayed in two layers of a fcc(111) lattice. To exclude the effect of line tension we consider cylindrically shaped droplets as can be seen in Fig. 1. In y -direction our domain is 48.6σ wide. We performed simulations with an approximately 40% wider and 40% smaller domain in y -direction which show practically identical results to confirm that the width is large enough to neglect finite-size effects and small enough to suppress Plateau-Rayleigh instabilities. The total amount of fluid particles is set to $N = 4 \cdot 10^4$ per droplet. To control the temperature we use a dissipative particle dynamics (DPD) thermostat [40, 41] in order to reproduce the correct hydrodynamics. In addition, we averaged every simulation setup over 50 trajectories to generate sufficient statistics.

To analyze the trajectories of the particles we first perform a projection along the y -axis so that we basically analyze a 2D-system (with axes x and z cf. Fig. 1).

A common procedure [42–44] to extract the droplet shapes from these projection is to calculate the density field first, then determine the position of the liquid gas interface for different heights z

and fit a circle to the obtained interface positions. Note that one cannot use circle fits due to the non-equilibrium nature of the underlying systems. Instead we calculate the position of the liquid vapor interface for every z -position by fitting the density with the function

$$\rho_z(x) = \frac{1}{2}(\rho_l + \rho_g) - \frac{1}{2}(\rho_l - \rho_g) \tanh\left(\frac{2(x - x_\beta(z))}{d_\beta}\right). \quad (2)$$

Here, $\rho(x)$, ρ_l and ρ_g are the particle density at position x , the density in the bulk and the density in the gas phase respectively. $x_\beta(z)$ gives the position of the liquid vapor transition by using a crossing criterion. The parameter d_β determines the width of the liquid-vapor interface. The same procedure can be applied for the perpendicular direction parallel to the z -axis to compute the liquid gas interface position z_β for a given x position. For our analysis we used the values of $x_\beta(z)$ for $z < h/2$ with a bin size of 1σ to average out layering effects and the values of $z_\beta(x)$ for $z > h/2$ where we use a bin size of 0.1σ . Here, h is the height of the droplet. Both methods can be consistently combined (cf. App. A) and help to resolve the droplet peaks better, because the fit is along a line with a significant share of particles in the liquid phase. Finally, we have chosen the height of the upper layer of the substrate to be at $z = -0.5\sigma$ since the particles have a diameter of σ , i.e. the top of the substrate particle is at $z = 0$.

B. Thin film equation theory (TFE)

The mesoscopic continuum model employed in this paper is based on the thin-film or lubrication approximation for the Navier-Stokes equation [30]. The lubrication approximation is given by an evolution equation of the local height $h = h(x, y, t)$, which can be written in a gradient dynamics form as [32, 45]

$$\partial_t h = \nabla \cdot \left[M(h) \nabla \frac{\delta \mathcal{F}}{\delta h} \right] \quad (3)$$

with the mobility $M(h)$ and the free energy functional $\mathcal{F} = \mathcal{F}[h]$. Here, we assume no-slip boundary conditions at the substrate leading to a mobility of $M(h) = h^3/(3\eta)$ with the dynamic viscosity η [30]. Several slip regimes can be accounted for by different choices for $M(h)$ [46]. The generalized pressure $P = \frac{\delta \mathcal{F}}{\delta h}$ is given by

$$P(h, x, t) = -\gamma \Delta h - \Pi(h, t) \quad (4)$$

with the surface tension γ and the disjoining pressure $\Pi(h, t)$. The latter is chosen as

$$\Pi(h, t) = \left(\frac{B}{h^6} - \frac{A}{h^3} \right) (1 + \rho(t)). \quad (5)$$

Here, A and B denote the interaction strengths of long and short ranging forces respectively, where A is directly connected to the Hamaker constant H by $A = H/6\pi$. A different choice of the disjoining pressure is possible, see e.g. [30, 34, 45] for details. In the present paper, the disjoining pressure in Eq. (5) is modulated by the parameter $\rho = \rho(t)$ to model switchable substrates, where ρ is a parameter corresponding to the wettability contrast. The use of the no-slip boundary condition at the substrate leads to a logarithmic energy dissipation at the contact line [31]. This singularity can be resolved by introducing a precursor film $h = h_p$ [31, 47], which is also present on macroscopically “dry” parts of the substrate. Alternate ways to resolve the singularity problem at the contact line are presented by Bonn *et al.* [31]. Note that a temporal modulation of the disjoining pressure as shown in Eq. (5) does not change the precursor film height [47].

In the following we employ the non-dimensionalized form of Eq. (3), where h , x and t are scaled in such a way, that 3η , γ , A and B are incorporated in the corresponding scaling (for details cf. App. B). This leads to the evolution equation

$$\partial_t h = \nabla \cdot \left\{ h^3 \nabla \left(-\Delta h - \frac{5}{3} \Theta_{\text{eq}}^2 \chi^2 \left(\frac{\chi^3}{h^6} - \frac{1}{h^3} \right) [1 + \rho(t)] \right) \right\} \quad (6)$$

with the equilibrium contact angle Θ_{eq} and the parameter $\chi = h_p/h_0$, where h_0 is the spatial scale. For further analysis we subtract the precursor film height h_p from the film height h in Eq. (6). Additionally, we keep $\Theta_{\text{eq}} = \sqrt{\frac{3}{5}}$ so that the effective equilibrium contact angle $\tilde{\Theta}_{\text{eq}}$ is determined by the parameter ρ as

$$\tilde{\Theta}_{\text{eq}} = \Theta_{\text{eq}} \sqrt{1 + \rho(t)}. \quad (7)$$

Note that the parameter χ can be regarded as a free parameter in this approach. The influence of this ratio on the equilibrium droplet shape is explained and visualized in App. C. In the following we use a value of $\chi = 0.01$, because smaller values of χ do not improve the agreements between both models in the contact region. Note that for different values of ρ the ratio of the precursor film height h_p to the maximum droplet height h_{max} does change for constant volume.

Note that the temperature does not enter the TFE model (6) directly, so that the temperature influence cannot easily be systematically analyzed. However, indirectly, the temperature enters the TFE model through the surface tension γ , the viscosity η and the particular shape of the disjoining pressure, which determines the wetting regime. In particular, the minimum of the inter-face potential (the integral of the disjoining pressure) is directly connected to the contact angle in the mesoscopic picture as a known disjoining pressure is sufficient to determine the equilibrium

state [31, 47]. Thus, the temperature in the mesoscopic thin-film model is automatically consistent with the particle-based MD model, if the droplet shapes match. Further influences of temperature is however outside the scope of this analysis.

The direct numerical simulations within the TFE model (6) are based on the finite element library oomph-lib[48]. In contrast to the MD model, cylindrically shaped droplets can directly be simulated on a one-dimensional (1D) domain in the thin-film model, which reduces the spatial dimension of the problem by one and directly excludes any instabilities possibly occurring in the transversal y -direction. In general, one can plug profiles from the MD model into the TFE model. As the MD model exhibits noise this requires small time steps in the simulation to reach a smooth profile. In some circumstances the time steps in the employed adaptive time stepping algorithm can get so small, that rounding errors of the machine can influence the results. To avoid such behavior we apply a filter to the MD data according to App.D before we start the simulation in the TFE model.

III. RESULTS

A. How to compare scales

In order to compare the scales in case of a static droplet, a mapping between ϵ_w and ρ responsible for the wettability in their respective models is necessary. For dynamic comparisons the time scales need to be mapped as well. In the first part of this section we describe the mapping in the static, equilibrium case and in the second part the mapping of time scales.

The relation of the liquid-solid interaction strength to the contact angle has been the focus of research for quite some time, e. g. Sullivan [49] came up with a qualitative theory on the base of a van der Waals model in 1981. This is closely related to the research on wetting transitions substantially advanced by [50–53]. Pandit *et al.* [50] investigated the wetting transition within a lattice-gas model for different interaction strengths and interaction ranges. Within the framework of a systematic van der Waals theory (mean-field model) critical wetting can also be observed[51]. Such critical wetting is non-generic as shown first by Dietrich and Schick [52].

Despite the efforts in this field there is no way to compute the relation between the interaction strength ϵ_w and the wettability parameter ρ without doing involved numerics. Even if possible, theories often only promise qualitative agreements[49], which is insufficient for our aim of a quan-

titative agreement in the dynamics of microscopic and mesoscopic models.

For the best agreement one could try to extract the exact shape of the disjoining pressure Π . As mentioned above, the disjoining potential has been extracted from MD simulations, lattice density functional theory (DFT), and continuum DFT [35–38]. This would give us even better agreements of the equilibrium droplet shapes. However, it is to note that some details of the extraction of wetting potentials are tricky and some open questions remain [38]. On the other hand, we have chosen the form in Eq. (5), so that we are automatically imposing the right wetting transition. Additionally, the parameter ρ enables us to change the minimum of the disjoining pressure Π , which enforces a certain equilibrium contact angle. This way we are able to isolate the single parameter ρ and can use it for a reliable, yet, empiric static mapping, so that we can take the next step and aim at a quantitative comparison not only of statics but of dynamics.

To map the interaction strength ε_w from the MD model to the parameter ρ from the TFE model we fix the volume and the temperature, so that we can fully classify a static droplet just by one parameter like the height or contact angle. Contact angles are hard to define and measure consistently in microscopic and mesoscopic models. The definition of the contact angle can have a strong influence and at the nanoscale contact angle can depend on the droplet size [54]. Indeed, in the mesoscopic TFE model the contact region is not represented accurately due to the lubrication approximation [31] and the contact line is hard to define due to the necessarily smooth transition to the precursor film. Consequently, it is not clear how results based on a contact angle mapping can be interpreted reliably. Figure 2 shows two mapped equilibrium profiles based on our mapping described in the following to give an idea, how the lubrication approximation (blue curve) influences equilibrium droplet shapes in the contact region.

Instead, we introduce *the relative full width at half maximum* rFWHM, which is defined as the height of the droplet divided by its width at half of the height. This parameter is not sensitive to the droplet shape in the contact region, while being sensitive to the overall shape. The measure rFWHM can be regarded as a computationally cheap way to estimate the curvature and thus is closely related to the contact angle. Another advantage of the rFWHM is that one can analyze the temporal evolution in a straight-forward manner. If one measures the contact angle by fitting the droplet shape with a spherical cap, the quality of the fit varies, because dynamic droplets do not necessarily have a spherical cap shape and thus the error margin of the measured contact angle changes.

We computed the equilibrium droplet shapes in both models and measured rFWHM in depen-

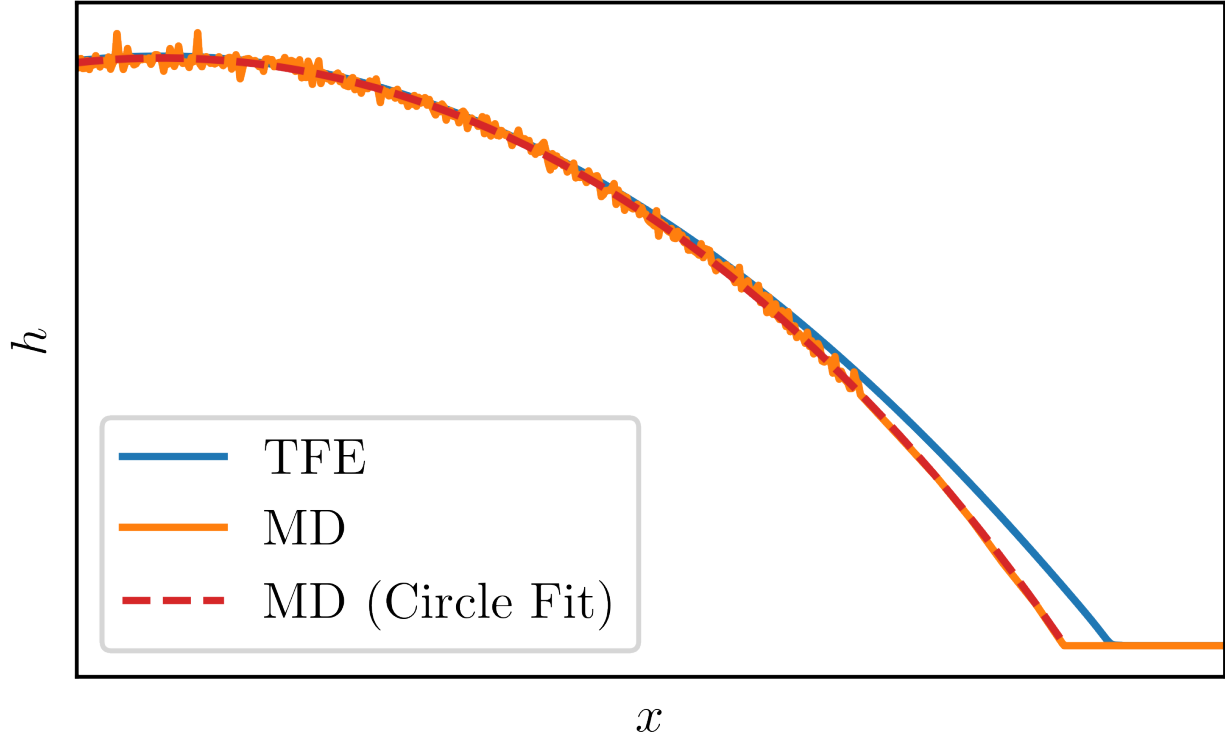


FIG. 2: Spatially rescaled height profiles of a static droplet from the MD and TFE model corresponding to $\varepsilon_w = 0.762$ and a circle fit to the height profile from the MD model.

dence of ε_w for the MD model and as a function of ρ for the TFE model. The rFWHM shows an approximately linear dependence of the interaction parameter squared ε_w^2 , so that we employed a linear fit to avoid a computationally costly parameter sweep with a higher resolution in ε_w . The low computational cost in the TFE model makes a detailed parameter sweep possible, so that linear interpolation can be used to compute the rFWHM for arbitrary values of ρ and vice versa. Combining both results yields a reliable, numerical mapping between ε_w and ρ as can be seen in Fig. 3. Detailed plots of $\varepsilon_w^2 \mapsto \text{rFWHM}$ and $\rho \mapsto \text{rFWHM}$ are shown in App. E.

For the mapping of the spatial scales the x - and z -coordinates can be simply normalized with the maximum height of the droplet in the corresponding model at a certain wettability. Here, the maximum height of a droplet on a surface with a wettability corresponding to $\varepsilon_w = 0.632$ in both models is used to scale the film height and the x -coordinates. In principle the scaling height can be chosen arbitrarily as long as it corresponds to the same height in both models, i. e. droplet height at a certain wettability.

A comparison of static droplet shapes from both models can be seen in Fig. 2. Both profiles

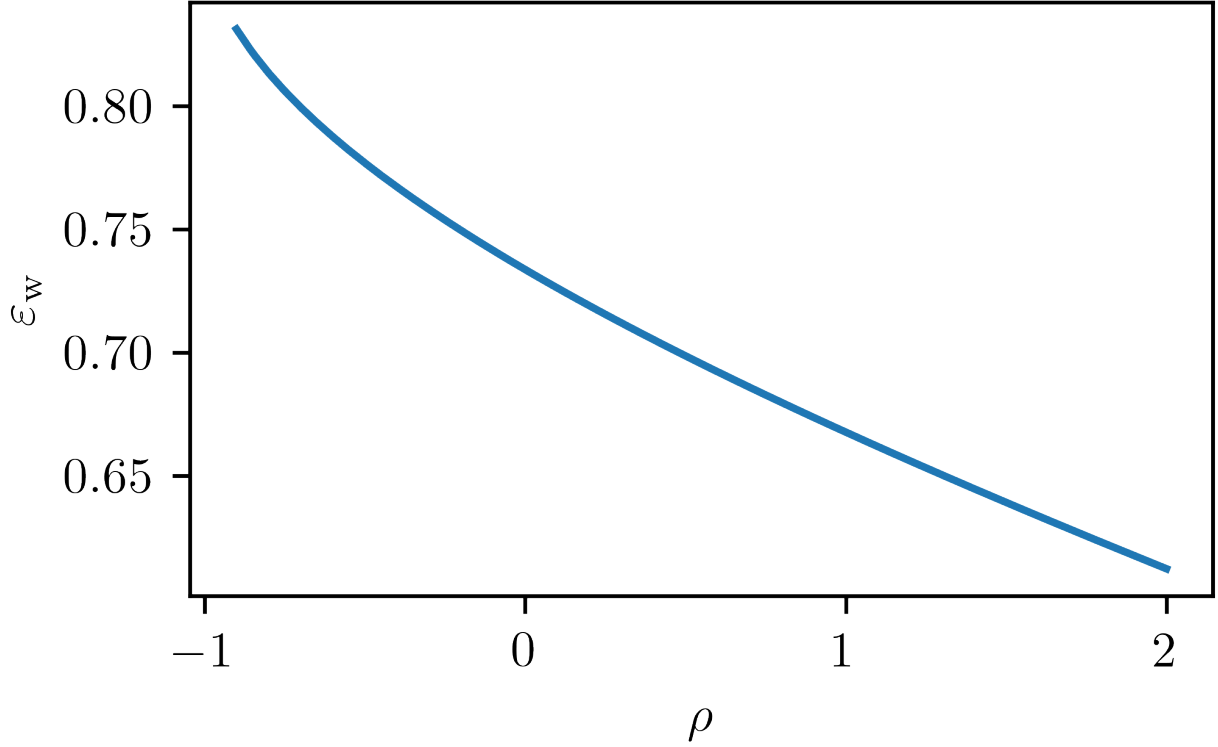


FIG. 3: Resulting mapping from the parameter ρ modulating the disjoining pressure in the thin-film picture to the interaction strength between solid and liquid ϵ_w in the MD model.

match well for heights of $h > 0.4h_{\max}$. As anticipated, there is some deviation in the contact region due to the lubrication approximation in the TFE model.

The mobility $M(h) = h^3/(3\eta)$ corresponds to a purely convective transport, which is expected to be the dominant transport mechanism. The mobility is important for dynamics, as it influences the pathway towards the minimum in the free energy[11]. In [55, 56] different mobility channels are discussed for other transport mechanism like diffusion. Before it is even possible to assess, whether a mobility has been chosen correctly, an adequate rescaling of the time for the comparison of the dynamics between MD and TFE model is necessary. In order to achieve a rather generic approach we compute the deviation from the TFE height profiles for every MD time step first. The deviation Δ is defined as

$$\Delta = \int_{h > 0.4h_{\max}} |h_{\text{MD}} - h_{\text{TFE}}| dx. \quad (8)$$

To exclude systematic errors originating from the lubrication approximation we only consider regions with $h > 0.4h_{\max}$. With the help of the computed deviations we can match every time step in the MD simulation to the time step of the TFE simulation with the least amount of deviation. In

App. E we show among other things, that the result for a cut-off of $h > 0.1 h_{\max}$ is fundamentally the same beyond higher noise. This results in a mapping $t_{\text{MD}} \mapsto t_{\text{TFE}}$. The mapping in this direction is more convenient as the MD model is a first principle model and uses a constant time step in contrast to the TFE model.

In the following we apply the resulting mapping to two different cases to demonstrate its applicability. First, we investigate the mapping for a liquid ridge, placed on a homogeneous, switchable substrate and secondly, we consider the mapping in the case of coalescence of two ridges. There we show that our mapping method can be applied universally and does not require additional simulations or measurements, where one had to worry about initial conditions influencing the measurement of a characteristic time.

IV. SINGLE SWITCH ON A HOMOGENEOUS SUBSTRATE

As a first example for the mapping procedure presented in Sec. III A we applied it to the dynamics of a one-dimensional ridge on a switchable substrate. The procedure for the simulations is as follows: The ridge is equilibrated at either high or low wettability ($\epsilon_{\text{HW}} = 0.762$ and $\epsilon_{\text{LW}} = 0.632$, respectively), before the wettability is instantaneously switched to the other wettability at $t = 0$.

Figures 4 a,b show the results of the mapping approach for switching towards higher and lower wettability, respectively. In both cases the data points of the mapping hardly deviate from a linear fit.

Notice that we discard the first few matched time steps for the fitting process due to two reasons. First, droplets in the MD simulations first adapt to a new wettability in the contact region and then changes near the droplet peak follow. Since we only consider regions with $h > 0.4 h_{\max}$ our mapping approach is not sensitive to these initial changes next to the contact region. For example, putting a droplet, equilibrated at a defined wettability on a surface with a higher wettability leads to an expansion of the droplet. Because of the broader droplet base (cf. Fig. 2) in the TFE model due to the lubrication approximation, the MD profile is likely to be matched to the equilibrium TFE profile within the first time steps. Second, for small timescales inertial effects can play a role which are not incorporated in the TFE model [30, 31]. Consequently, a linear fit of the mapping does not go directly through the origin. Additionally a cut-off for large times needs to be introduced, as soon as changes in the droplet profile between time steps are dominated by noise in the MD model.

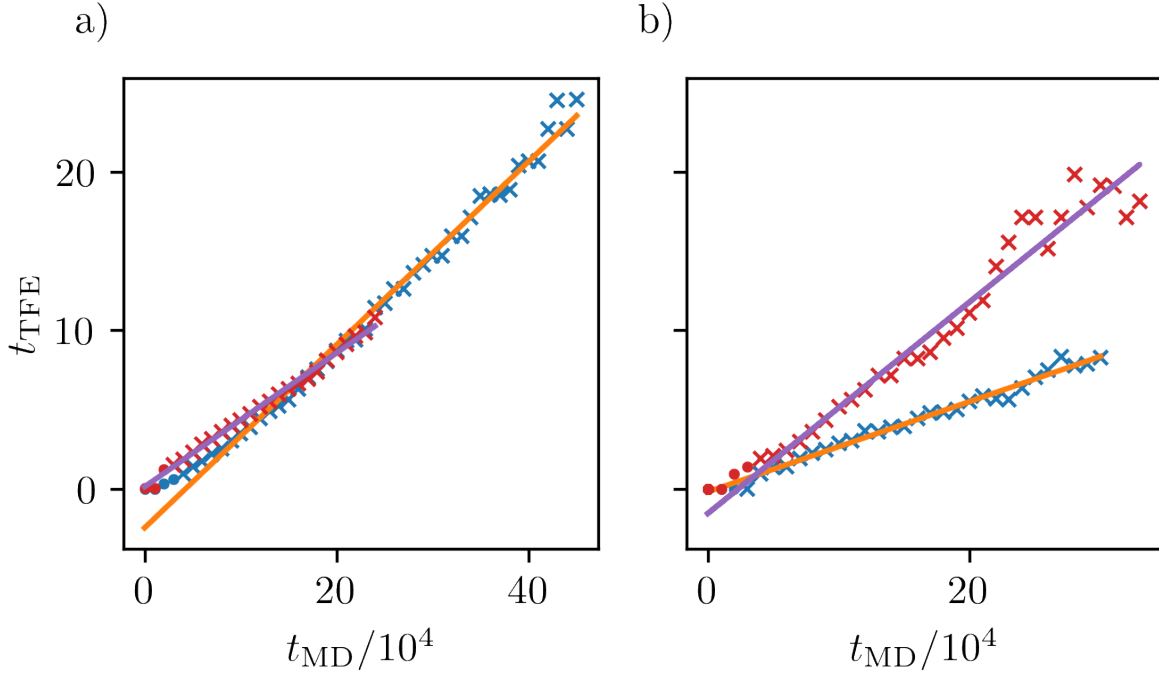


FIG. 4: Result of the mapping approach applied to a) the switching from ϵ_{LW} to ϵ_{HW} (blue data points and orange linear fit) and vice versa (red data points and violet linear fit) and b) the switching from $\epsilon_w = 0.671$ to $\epsilon_w = 0.707$ (blue data points and orange linear fit) and from $\epsilon_w = 0.671$ to $\epsilon_w = 0.707$ (red data points and violet linear fit). Crosses and dots show data points of matched profiles, whereas the solid line is a linear fit only considering the crosses. Dots are data points discarded for the linear fit.

The space-time representations in Fig. 5 show the evolution of the film profile $h(x, t)$ as the ridge adapts to the new wettability. The colormap indicates the film height. The results from both models look very similar in this representation. Besides the noise in the MD model the offset for the switch towards higher wettability accounts for the only general difference. This offset is a consequence of the previously described effect of the intermediate initial assimilation. To better grasp how good the models compare, the change of the height in time at three distinct points in space is shown in Fig. 6. For the direct comparison between the models times from the TFE model are converted into MD units t_{MD} .

For both switching directions the evolution for the height at points I and II is in a close agree-

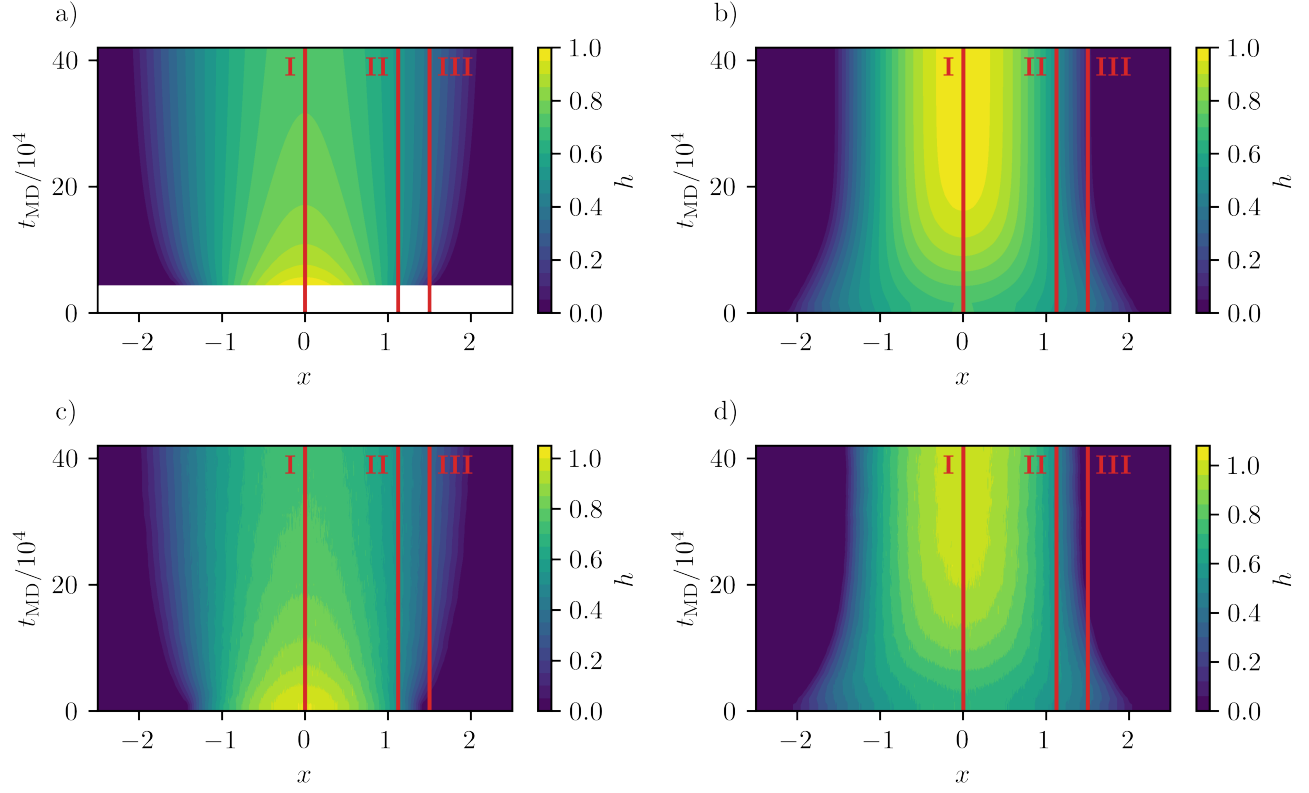


FIG. 5: Space-time plots showing the evolution of the height profile after a change in wettability for $\varepsilon_{\text{HW}} = 0.762$ and $\varepsilon_{\text{LW}} = 0.632$. a) and c) switch from low to high wettability in the TFE and the MD model, respectively. b) and d) show inverse switching direction in the TFE and the MD model, respectively. Red vertical lines labeled I, II and III indicate at which positions the height profile evolution is shown in Fig. 6.

ment between the models. The situation is however a bit different for point III. After an initial close agreement the deviations grow significantly (cf. Fig. 6). This behavior can easily be explained since already static ridges from both models do not match well in the region located close to the contact line (cf. Fig. 2). The reason is the underlying lubrication approximation in the TFE model, which results in higher film heights in the contact region compared to the MD model. Note that the mapping procedure also holds for different temperatures as can be seen in App. F

Interestingly, one finds a position, where the height profile behaves non-monotonically. In particular, for point II the film height increases first and then decreases to its equilibrium value. This effect occurs for both switching directions, although it is more pronounced, when switching from high to low wettability. The dotted black lines in Fig. 6 help to grasp this phenomenon. Finding such a distinct behavior barely distinguishable from noise, confirms that the parameters

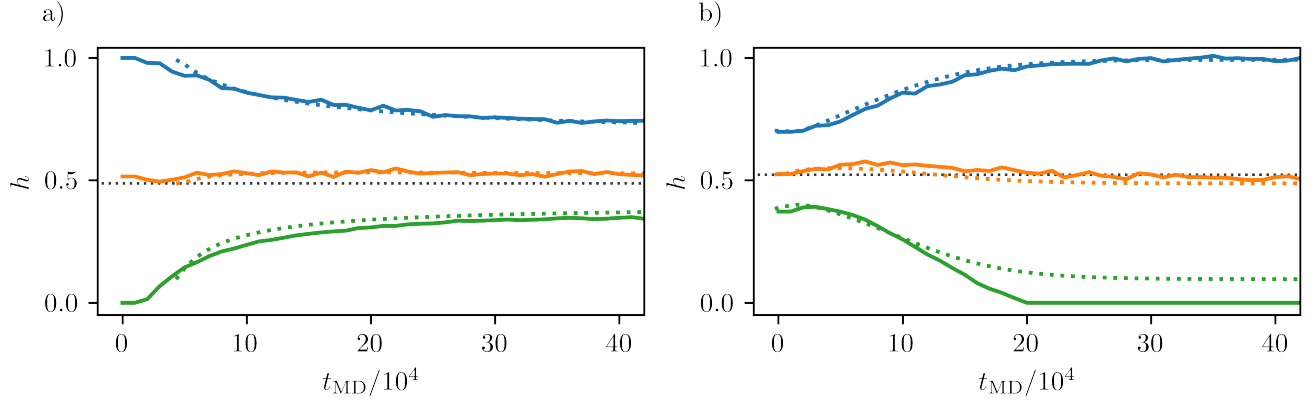


FIG. 6: Three characteristic height profiles along the marked lines I (blue), II (orange) and III (red) as shown in Figure 5. The height profiles extracted from the MD model are presented with solid lines. The dotted lines are TFE results with the temporal scaling obtained using our mapping approach. The height h is given relative to the maximum height. The black dotted line indicates the initial height in the TFE model for slice II to emphasize the non monotonous behavior for the height profile at this position. a) the wettability is switched from low to high, b) the wettability is switched in the opposite direction.

are chosen in such a way, that both models show consistent behavior.

Table I shows resulting time scale ratios (corresponding to the slope of the linear fit) for the switching process between different wettabilities. It becomes apparent that the time scale ratios have to be determined individually for every simulation. Unexpectedly, this seems to be the case for a similar target wettability as well, e. g. for the target wettability $\varepsilon_w = 0.707$ a time scale ratio $R_{f_{\text{LW} \rightarrow \text{HW}}} = 3.04 \cdot 10^4$ is computed for an initial lower wettability of $\varepsilon_w = 0.671$ as well as a ratio of $R_{f_{\text{HW} \rightarrow \text{LW}}} = 1.70 \cdot 10^4$ starting from a wettability of $\varepsilon_w = 0.743$ (compare also Fig. 4). The main difference in these simulations is the underlying physical process. Switching towards a lower wettability means, that the contact angle increases, which means the ridge is contracting. For the opposite direction the contact angle decreases and spreading can be observed.

Note that as shown in [57], the dynamics is affected by dissipation inside a liquid wedge of the droplet as well as by molecular features. The velocity of the contact line and the contact angle determine, how much dissipation and molecular features contribute to the dynamics. Since the TFE model cannot account for molecular features, discrepancies in the time scales arise.

TABLE I: Comparison of time scale ratios for different wettabilities and wettability differences computed with our mapping approach.

ϵ_{LW}	ϵ_{HW}	$R_{f_{\text{HW} \rightarrow \text{LW}}}$	$R_{f_{\text{LW} \rightarrow \text{HW}}}$
0.632	0.671	$1.55 \cdot 10^4$	$3.62 \cdot 10^4$
0.671	0.707	$1.67 \cdot 10^4$	$3.04 \cdot 10^4$
0.707	0.742	$1.70 \cdot 10^4$	$2.12 \cdot 10^4$
0.632	0.762	$2.37 \cdot 10^4$	$1.71 \cdot 10^4$

V. COALESCENCE OF TWO RIDGES

As a second test case for the quality of the mapping procedure between the MD and TFE models we investigated the coalescence of two ridges on a homogeneous substrate. To get an input geometry a ridge on a surface with a wettability of $\epsilon_w = 0.707$ is equilibrated in a MD simulation. A copy is then translated in x -direction in such a way, that it has a distance of 0.5σ from the primary ridge at the contact line. To maintain the particle density we further extended the MD system (and thus the surface) in the x -direction by a factor of two. From this MD input geometry we calculated the positions for the liquid-vapor-transition of the two ridges and used this data as an input for the TFE simulations.

The spatial rescaling from the single switch experiments can be employed without further issues. The result of our temporal mapping can be seen in Fig. 7. One can observe that in this cases the relation between both models cannot be reasonably fitted with a single linear function. Instead, a piece-wise linear function is well suited to represent the data. We divided the data points where we perceived the kink visually. In Fig. 7 the colors of the linear fits match the data points used for fitting. The intersection of the linear functions is at $t_{\text{MD}} = t_c = 18.1 \cdot 10^4$. Figure 7 visualizes, which times correspond based on our time scale mapping.

In particular, the time t_c corresponds to the time at which there is no longer a local minimum in the height profiles, i.e. the time at which the merging process of both droplets is completed. Plots of the height profile can be found in App. G. After t_c is reached, the droplet still contracts further. The time scale ratios are $R_{f_{\text{coal},1}} = 3.79 \times 10^4$ in the first part and $R_{f_{\text{coal},2}} = 1.70 \times 10^4$ in the second part. Compared to the ratios in Tab. I, where the wettability is switched towards $\epsilon_w = 0.707$, it strikes that we computed a ratio of $R_{f_{\text{LW} \rightarrow \text{HW}}} = 3.04 \cdot 10^4$ for switching towards higher wettability

(spreading droplet) and a ratio of $R_{f_{\text{HW}} \rightarrow \text{LW}} = 1.70 \cdot 10^4$ (contracting droplet). In the first part of the coalescence the two droplets spread in the sense, that the droplet peaks shrink in height and the connecting bridge grows. In the second part the merged droplet contracts and evolves towards the equilibrium configuration. This indicates, that it is consistent to find two time scale ratios in the coalescence.

Generally, we suspect that two time scales can be observed here, because physically different phenomena (coalescence and equilibration on a homogeneous substrate) play the decisive role in both parts of the dynamics. It is also likely that an initial solution in the TFE model directly taken from the MD model encourages these deviations, because the differences in the contact region lead to an initial state in the TFE model, which is farther away from the equilibrium state than the initial state in the MD model. Consequently, the evolution could be artificially accelerated until the droplets have merged. Additional simulations with initial droplet profiles taken from droplets equilibrated within the TFE model at the same peak distance still showed a nonlinear time scale relation. This underlines our hypothesis, that this is due to the different physical phenomena involved and differently affected by the lubrication approximation in the TFE model.

Despite not showing a linear relation over the whole simulation the mapping can be used to compare the dynamics in both models. Figure 8 shows a space-time plot representation of the coalescence. The evolution of the height profile at three distinct points can be seen in Fig.9.

Again, the results match very well except for the anticipated difference at the contact region. The good agreement in Fig. 9 is only possible, because we allow a shifted zero of the time scales, i. e. we do not force that $t_{\text{MD}} = 0$ is the start of the TFE simulation.

VI. CONCLUSION

In this paper we have presented a first step towards the quantitative comparison between the microscopic MD and the mesoscopic TFE model for the dynamics of liquid droplets. In a first step the parameters responsible for the substrate wettability in the respective models are mapped for equilibrium droplets. Thereby a mapping between the spatial quantities is achieved. In the second step, the general approach for the mapping of the time scales on the basis of matched droplet shapes is applied. The applicability of the presented approach is shown thoroughly for two examples, a droplet on a homogeneous, switchable substrate and the coalescence of two droplets. We have demonstrated, that intermediate steps in the evolution are in good agreement. This implies, that

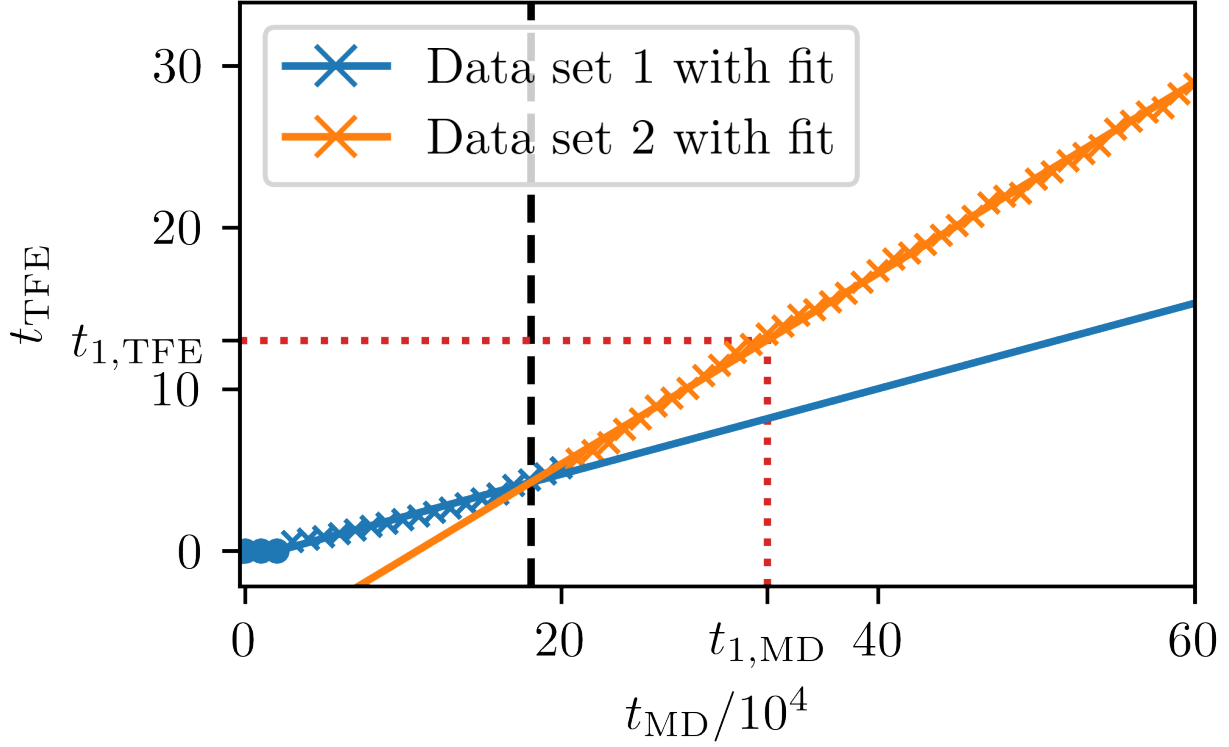
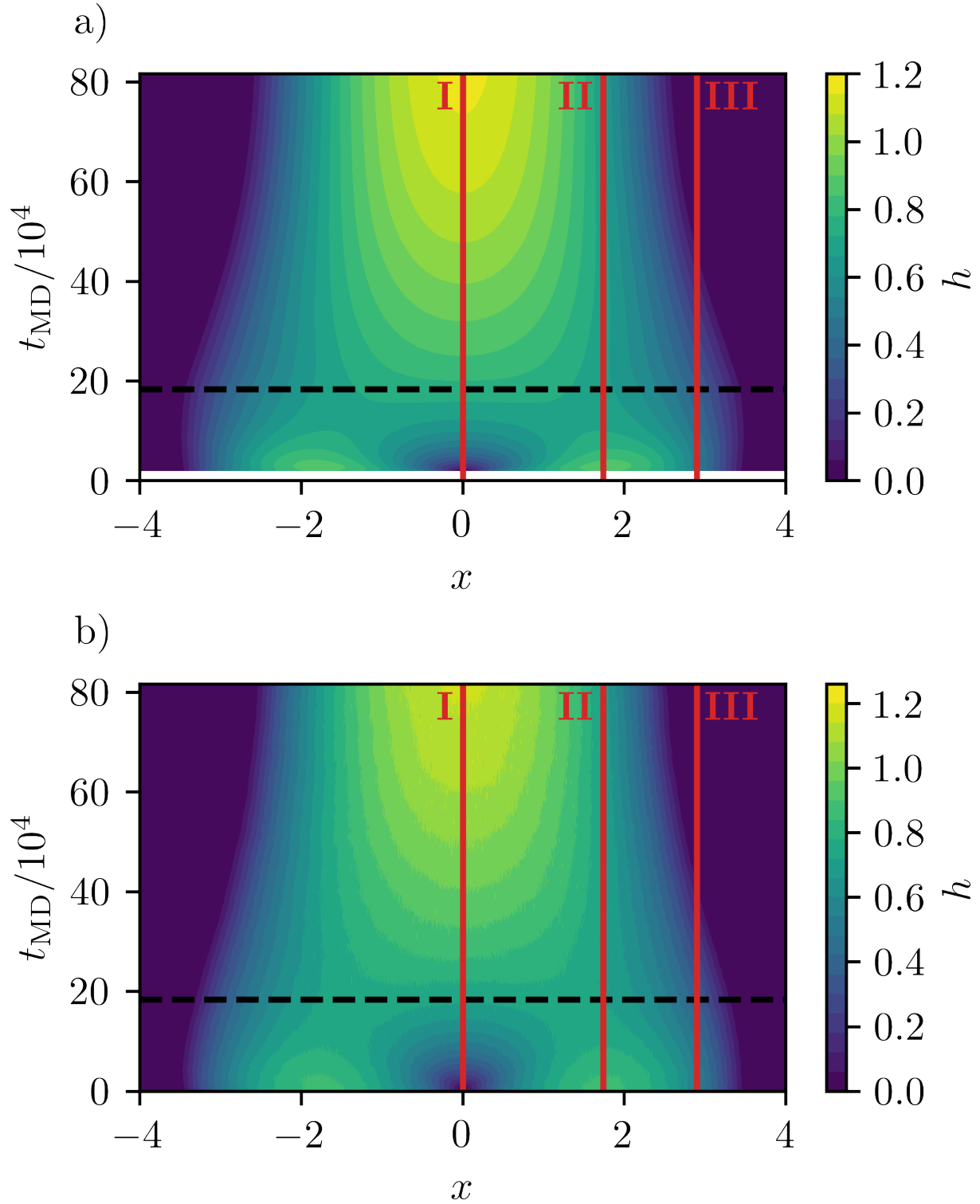


FIG. 7: Result of the temporal mapping for the coalescence of two ridges. Data points of the matched profiles are shown as crosses. Only the crossed data points in matching colors are considered for the corresponding fit shown as a solid line. Two distinct time scales can be observed, both fitted with a linear function. The slopes are $a_1 = 0.0264 \pm 0.001$ and $a_2 = 0.05892 \pm 0.0003$. This corresponds to timescale ratios of $R_{f_{coal},1} = 3.79 \cdot 10^4$ and $R_{f_{coal},2} = 1.70 \cdot 10^4$ respectively.

the same path in phase space is taken in both models. This can be attributed to our reliable mapping of the parameters ε_w and ρ responsible for the wettability in their respective models.

Note that our mapping can always be applied, as long as one stays within the limits of the TFE models, i. e. low contact angle and concept of a precursor film. If one keeps the limits in mind, computational resources can be saved, because it enables one to accurately find the parameter range of interest in the TFE model and perform simulations on the mesoscopic scale. The other direction is also possible, e. g. some interesting behavior is found within the TFE model and the MD model can provide microscopic insights of the dynamics. The presented approach is not specially tailored to the employed thin-film model. An application of the presented mapping approach for a continuum model, which allows for larger contact angles (e. g. macroscopic bound-



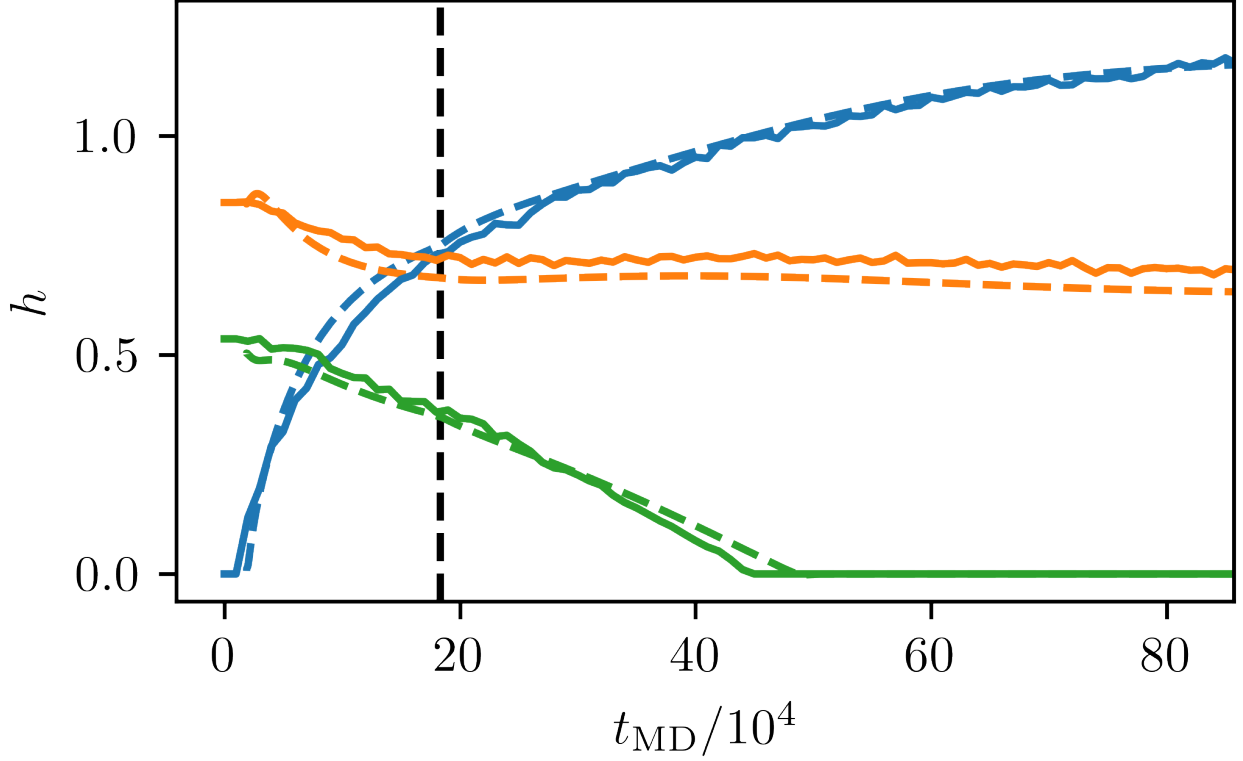


FIG. 9: Three characteristic height profiles along the marked lines in Fig. 8. The height profiles extracted from the MD model are represented with solid lines, whereas the height profiles from the TFE model are dashed. The scaling is the same as in Fig. 8.

any element method [25]), is also possible. Mapping to continuum models additionally promises fruitful results with the help of bifurcation analysis, which can help predict onsets of instabilities or explore large parameter spaces systematically along stable branches.

The procedure presented here additionally can help to reduce computational demands, as a simulation in the MD model can be continued within the TFE model, which is much more efficient, while still featuring the same quantitative non-equilibrium time evolution.

A universal time scale factor, which works for switching in both directions as well as for other wetting phenomena, has not been found. For example, we computed different time scale ratios for the very same substrate wettability, i. e. the same final state, by merely changing the initial state (cf. Tab. I). However, even if two different scaling regimes are present, the mapping of the times can be obtained in a generic manner. Thus, our rescaling approach provides a possibility to map the time scales, if characteristic times are not easily and reliably accessible.

In the future, our approach for the time scale comparison could be extended to a thin-film

model with a fine-tuned disjoining pressure. Literature provides ample opportunities to extract the disjoining pressure directly from microscopic models, which enables comparisons between models in the static case[35–38, 58–61] but not for dynamics. However, the presented empirical static mapping matched the most important characteristics of the disjoining pressure to the MD model, i. e. we made sure, that the minimum of the interface potential was correct, that the precursor film height was chosen adequately (cf. App. C) and that the wetting regime was correctly mirrored by our disjoining pressure. Finally, the presented mapping was performed under the assumption of the no-slip boundary condition at the substrate leading to the cubic mobility in the thin film model. Although the mapping shows extremely good agreement but in the contact line region, the role of different mobility channels (e.g., weak and intermediate slip or diffusion of the entire adsorbed film) onto the time scale mapping is the subject of future work.

In the accompanying zenodo dataset [62] we provide the simulation data, the code to reproduce the figures and the oomph-lib code to perform the simulations in the TFE model.

ACKNOWLEDGMENTS

We wish to acknowledge the financial support of the DFG Schwerpunktprogramm SPP 2171.

Appendix A: Droplet shapes

Figure 10 shows the position of the liquid vapor interface x_β and z_β , respectively, calculated with eq. 2 from the MD simulations plotted against the x -coordinate of the system. For z_β a bin width of 0.1σ is used. For x_β a bin width of 1σ is used to average out layering effects.

Appendix B: Nondimensionalization

The thin-film equation with dimensioned variables reads

$$\partial_t h = \nabla \left[\frac{h^3}{3\eta} \nabla \frac{\delta F}{\delta h} \right] \quad (\text{B1})$$

$$\frac{\delta F}{\delta h} = -\gamma \Delta h - \left(\frac{B}{h^6} - \frac{A}{h^3} \right) (1 + \rho(t)). \quad (\text{B2})$$

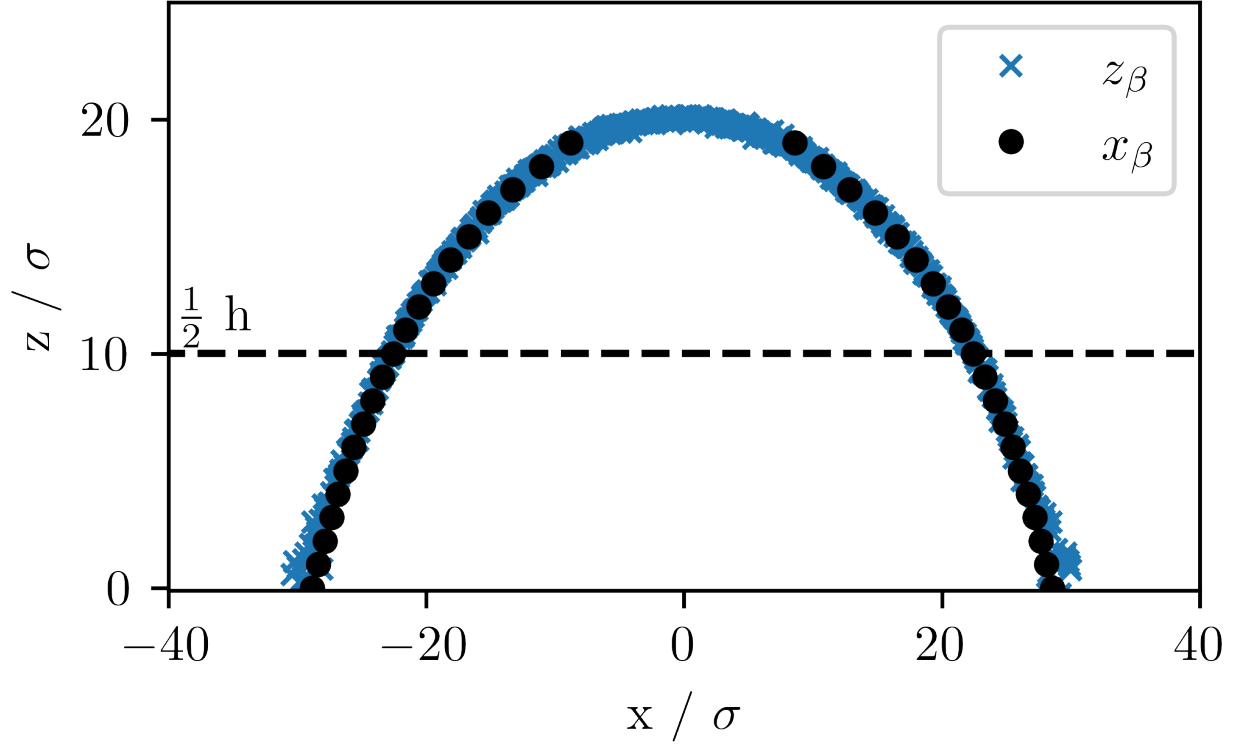


FIG. 10: Position of the liquid vapor interface obtained from fits parallel x_β and perpendicular to the substrate z_β .

For a given disjoining pressure Π the precursor film height is defined as the minimum of the interface potential, which is defined as

$$I = - \int \Pi dh = \left[\frac{B}{5h^5} - \frac{A}{2h^2} \right] (1 + \rho(t)). \quad (\text{B3})$$

The minimum of the interface potential is the zero of the disjoining pressure, which leads to

$$\frac{A}{h_p^5} - \frac{B}{h_p^3} = 0 \quad \Rightarrow \quad h_p = \left(\frac{B}{A} \right)^{\frac{1}{3}} \quad (\text{B4})$$

In the context of the lubrication approximation the relation

$$\Theta_{\text{eq}} = \sqrt{\frac{-2I(h_p)}{\gamma}} \quad (\text{B5})$$

holds, which defines the equilibrium contact angle Θ_{eq} for a given interface potential I , surface tension γ and precursor film height h_p . Combining Eq. (B4) and Eq. (B5) yields the relations

$$A = \frac{5}{3} \gamma \Theta_{\text{eq}}^2 h_p^2 \quad \text{and} \quad B = \frac{5}{3} \gamma \Theta_{\text{eq}}^2 h_p^5 \quad (\text{B6})$$

for the constants A and B . Plugging these into Eq. (B2) gives

$$\frac{\delta F}{\delta h} = -\gamma\Delta h - \frac{5}{3}\gamma\Theta_{\text{eq}}^2 h_p^2 \left(\frac{h_p^3}{h^6} - \frac{1}{h^3} \right) (1 + \rho(t)). \quad (\text{B7})$$

Then we introduce the scales

$$x \rightarrow x_0 \cdot \tilde{x}, \quad t \rightarrow t_0 \cdot \tilde{t}, \quad h \rightarrow h_0 \cdot \tilde{h}, \quad \frac{\delta F}{\delta h} \rightarrow F_0 \cdot \frac{\tilde{\delta F}}{\tilde{h}} \quad (\text{B8})$$

and insert them into the dimensioned thin-film equation. After dropping the tildes we get

$$\partial_t h = \nabla \left[\frac{h_0^2 t_0 F_0}{3\eta x_0^2} h^3 \nabla \frac{\delta F}{\delta h} \right] \quad (\text{B9})$$

$$\frac{\delta F}{\delta h} = -\frac{\gamma h_0}{x_0^2 F_0} \Delta h - \frac{5\gamma\Theta_{\text{eq}}^2 h_p^2}{3F_0 h_0^3} \left(\frac{h_p^3}{h_0^3} \frac{1}{h^6} - \frac{1}{h^3} \right) (1 + \rho(t_0 t)). \quad (\text{B10})$$

The scales x_0 , h_0 , t_0 and F_0 can be chosen freely. Here, the parameter h_0 is used as a reference height, which can be an experimentally measured droplet size. We can then simplify the thin-film equation by solving

$$\frac{h_0^2 t_0 F_0}{3\eta x_0^2} = 1 \quad (\text{B11})$$

$$\frac{\gamma h_0}{x_0^2 F_0} = 1 \quad (\text{B12})$$

$$\frac{5\gamma\Theta_{\text{eq}}^2 h_p^2}{3F_0 h_0^3} = \frac{5}{3}\Theta_{\text{eq}}^2 \chi^2, \quad (\text{B13})$$

where we have introduced $\chi = h_p/h_0$. Solving this system of equations for the scales eliminates most of the prefactors. Keeping the term $\frac{5}{3}\Theta_{\text{eq}}$ ensures that all the spatial dimensions are scaled similarly. The solution is

$$x_0 = h_0, \quad t_0 = \frac{3\eta h_0}{\gamma}, \quad F_0 = \frac{\gamma}{h_0}. \quad (\text{B14})$$

With these scales the thin-film equation can finally be written as

$$\partial_t h = \nabla \left[h^3 \nabla \frac{\delta F}{\delta h} \right] \quad (\text{B15})$$

$$\frac{\delta F}{\delta h} = -\Delta h - \frac{5}{3}\Theta_{\text{eq}}^2 \chi^2 \left(\frac{\chi^3}{h^6} - \frac{1}{h^3} \right) (1 + \rho(t)). \quad (\text{B16})$$

In this form the temporal modulation of the disjoining pressure $\rho(t)$ is expressed in the dimensionless units. A more detailed derivation of the non-dimensionalization is presented by Engelinkemper[47].

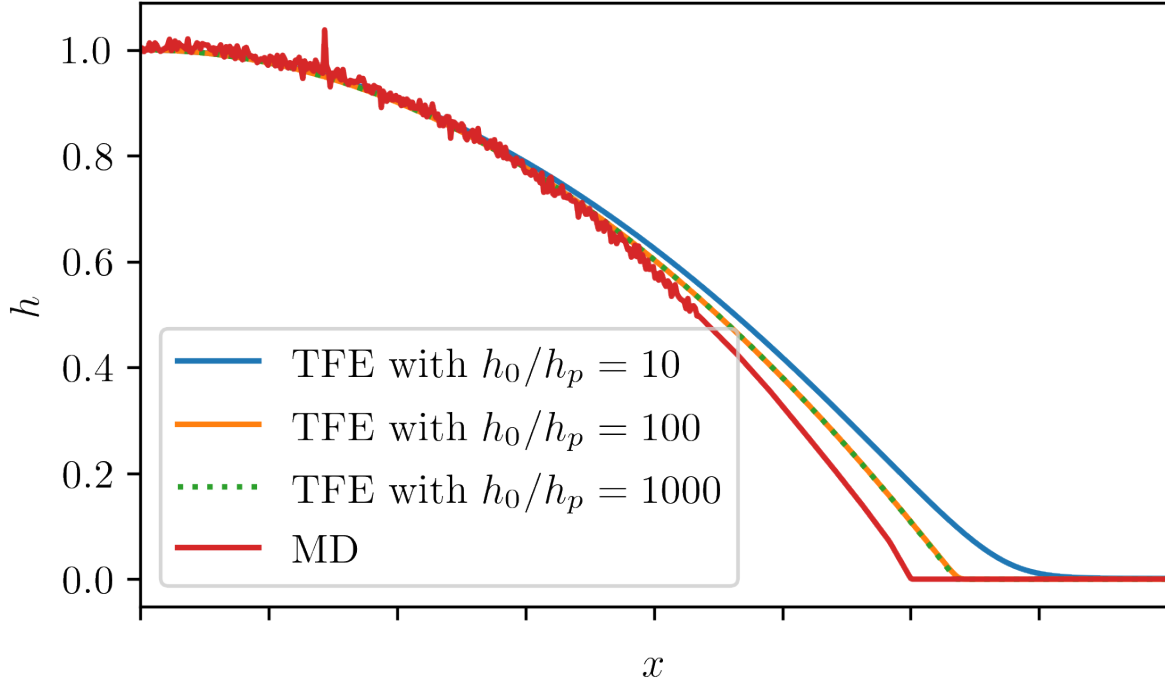


FIG. 11: MD profile plotted on top of profiles from TFE simulations with different ratios of droplet height to precursor film height. Here, droplet height h_{\max} is chosen to be h_0 .

Appendix C: Influence of the ratio h_{\max}/h_p

Figure 11 shows how the ratio of droplet height to precursor film height affects the resulting droplet shape. The deviations of the profile with $h_{\max}/h_p = 10$ from the profile with $h_{\max}/h_p = 100$ can be explained by a necessarily smooth transition from droplet to precursor film. The effect is reduced if the precursor film height is smaller. The effect of the lubrication approximation becomes apparent, when the MD profile is compared to the TFE profile with the highest ratio of droplet height to precursor film height shown. Figure 11 shows that the droplet profile converges for $\chi = h_p/h_0 \rightarrow 0$. A higher value of χ makes computation faster, because the discretisation in space can be increased. Our choice $\chi = 0.01$ is sufficiently close to the profile for $\chi = 0.001$ whilst being roughly 10 times computationally cheaper with regards to memory and processing speed. The noise of the MD profile in the contact region is smaller compared to the peak of the droplet, because the fitting direction to determine the interface is changed. If we did not change the fitting direction, we would have a badly resolved droplet peak. Appendix A visualizes, how the interface position is determined.

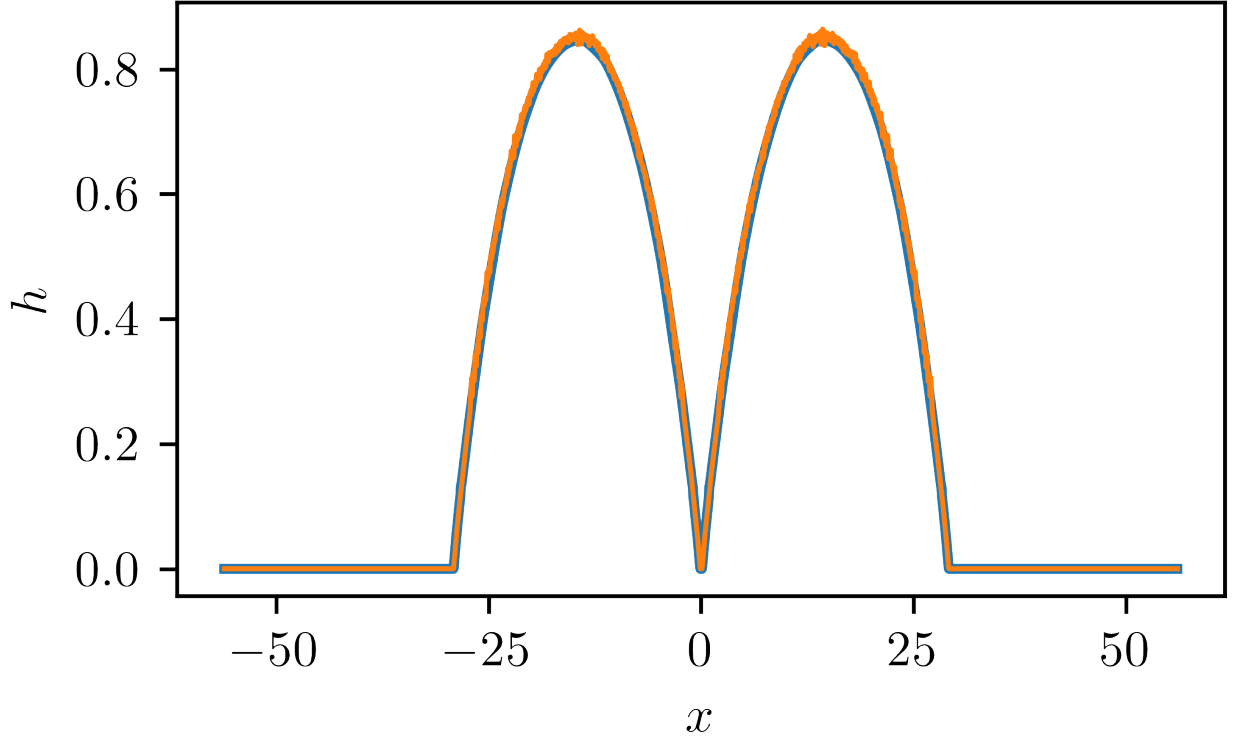


FIG. 12: Comparison of the height profile directly extracted from the MD model and the height profile after a LOWESS filter was applied to the parts of the MD data, where $h > 20h_p$.

Appendix D: Filter noise from MD profiles

Before a height profile from the MD model is plugged into the TFE model the noise is reduced on the height profile by averaging over 50 runs. Some noise still persists, which can lead to very small time steps in the TFE model possibly leading to inaccurate results due to rounding errors caused by the finite computational accuracy. Figure 12 shows the difference between the filtered and the unfiltered data. We applied the LOWESS (Locally Weighted Scatterplot Smoothing) filter from the python package statsmodel[63] to the height profile and only exchanged the data points with a height above 20 times the precursor film height. Otherwise the contact region would have been altered too much and noise in the contact region is low compared to the droplet peaks.

Appendix E: Addendum for subsection III A

Figures 13 and 14 visualize the intermediate steps to achieve the result shown in Fig. 3.

The choice of the criterion, which determines the data points of the height profiles to be con-

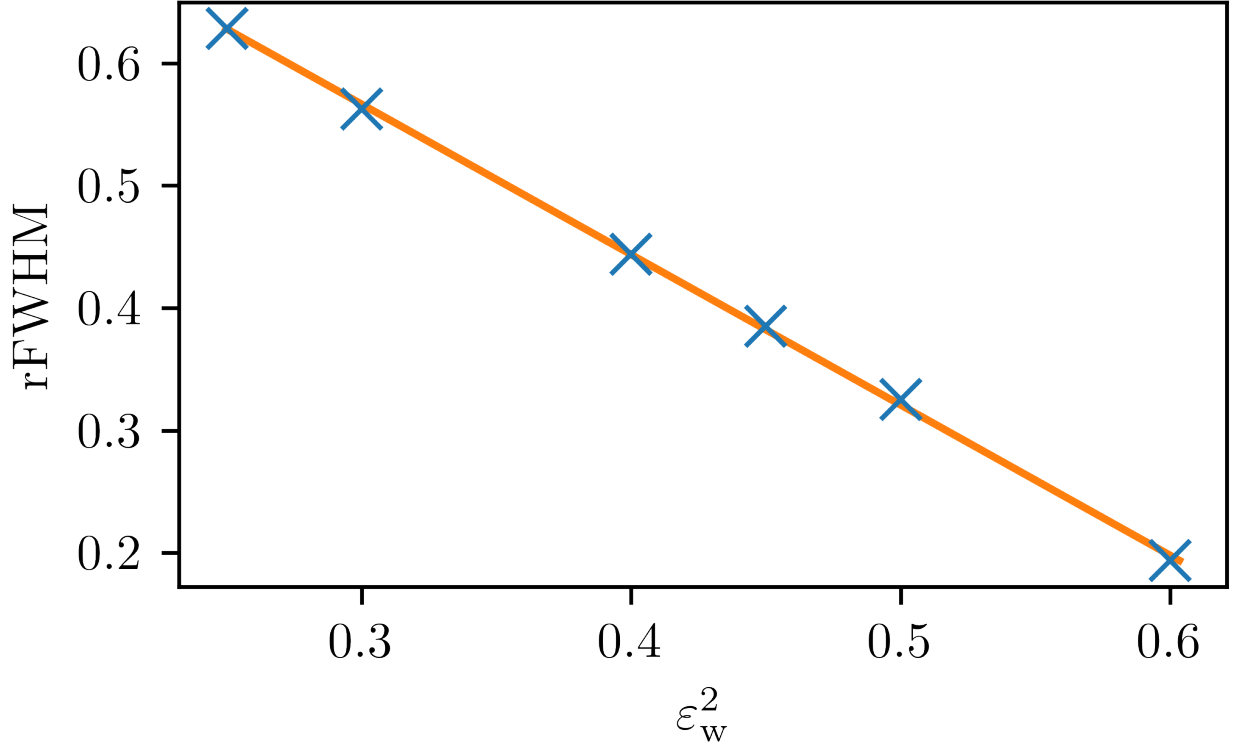


FIG. 13: Linear fit of the squared interaction strength ε_w^2 depending on the rFWHM with the function $\varepsilon_w^2(\text{rFWHM}) = (\text{rFWHM} - b)/a$. The fit parameters are $a = -0.814 \pm 0.009$ and $b = 0.761 \pm 0.004$. This linear fit is used for the mapping $\rho \mapsto \varepsilon_w$ shown in Fig. 3 and the inverse direction.

sidered, does not have a big impact. Figure 15 shows the result, when only data points with $x \in [-0.1, 0.1]$ are considered. The overall slope is close to the result shown in Fig. 4. However, the variance in the data points explains, why the criterion $h > 0.4h_{\max}$ is the preferred choice.

Appendix F: Temperature dependence of the mapping procedure

For different temperatures the general shape of the mapping curve between ε_w and ρ is approximately the same and just shifted to higher values of ε_w as can be seen in Fig. 16. It demonstrates, how the temperature enters the TFE model implicitly.

Also the dynamic mapping approach can be used for other temperatures as can be seen in the space time plots and the slices in Fig. 17 and Fig. 18 where the results from MD and TFE simulations are shown for $T = 0.70$.

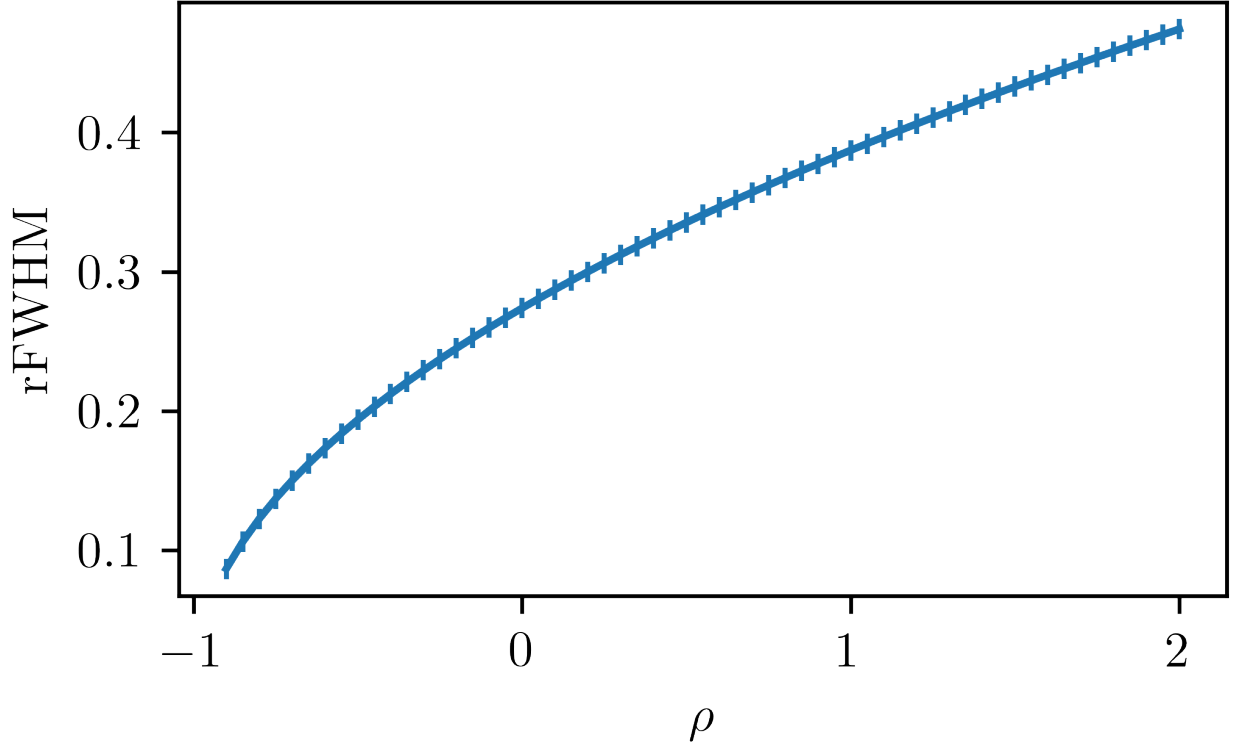


FIG. 14: Dependency of the rFWHM on the parameter ρ . Vertical bars indicate the resolution of the parameter sweep used for a linear interpolation in the mapping $\rho \mapsto \varepsilon_s$.

Appendix G: Matched profiles when comparing time scales

Figure 19 shows two matched height profiles according to the procedure in Sec III A for the coalescence simulations investigated in Sec. V. The deviation at the contact region is expected as a consequence of the lubrication approximation. The matched profiles on the right correspond to the critical time t_c , where both linear fits intersect in Fig. 7.

-
- [1] M. K. Chaudhury and G. M. Whitesides, How to make water run uphill, *Science* **256**, 1539 (1992).
 - [2] H. Gau, S. Herminghaus, P. Lenz, and R. Lipowsky, Electrochemical principles for active control of liquids on submillimeter scales, *Science* **283**, 46 (1999).
 - [3] B. Yoon, H. Acharya, G. Lee, H.-C. Kim, J. Huh, and C. Park, Nanopatterning of thin polymer films by controlled dewetting on a topographic pre-pattern, *Soft Matter* **4**, 1467 (2008).

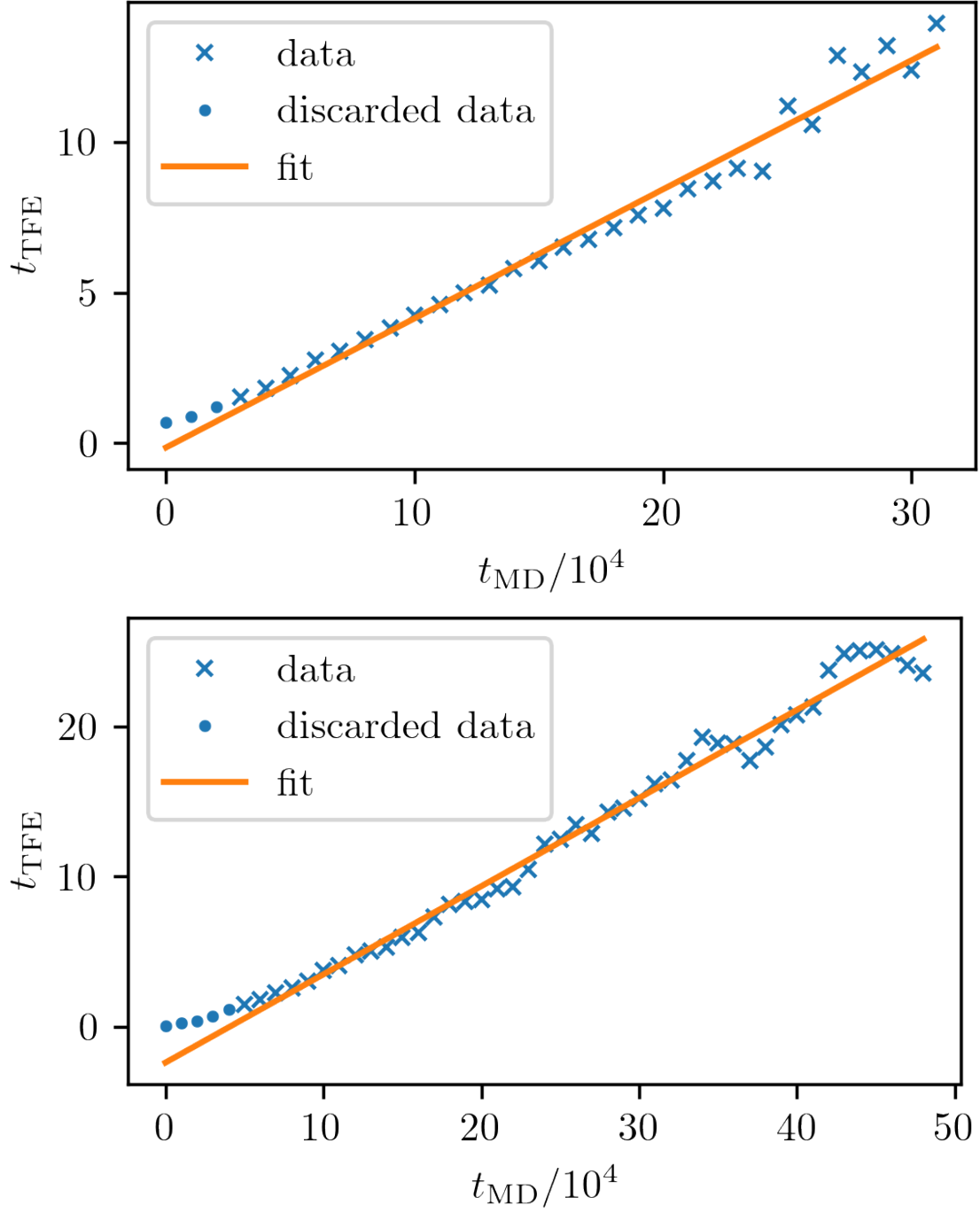


FIG. 15: Result of our rescaling approach applied to switching from high to low (top) and low to high (bottom) wettability. Here, only the data points with $x \in [-0.1, 0.1]$ are considered for the mapping to show the robustness of our approach regarding the choice of data points to be considered.

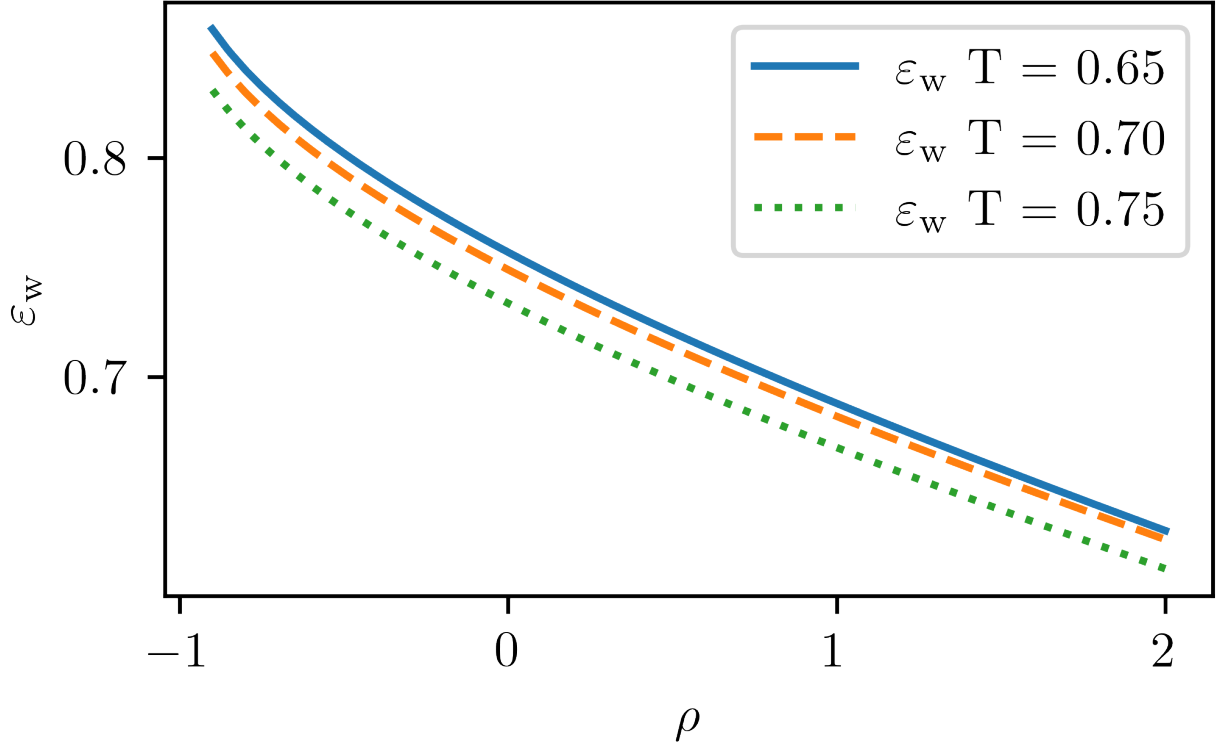


FIG. 16: Static mapping between ε_w and ρ for temperatures 0.65, 0.70 and 0.75.

- [4] R. Seemann, M. Brinkmann, E. J. Kramer, F. F. Lange, and R. Lipowsky, Wetting morphologies at microstructured surfaces, *Proceedings of the National Academy of Sciences* **102**, 1848 (2005), <https://www.pnas.org/content/102/6/1848.full.pdf>.
- [5] W. Wang, C. Du, C. Wang, M. Hirtz, L. Li, J. Hao, Q. Wu, R. Lu, N. Lu, Y. Wang, H. Fuchs, and L. Chi, High-resolution triple-color patterns based on the liquid behavior of organic molecules, *Small* **7**, 1403 (2011), <https://onlinelibrary.wiley.com/doi/pdf/10.1002/sml.201002210>.
- [6] J. Zhu, M. Wilczek, M. Hirtz, J. Hao, W. Wang, H. Fuchs, S. V. Gurevich, and L. Chi, Branch suppression and orientation control of langmuir-blodgett patterning on prestructured surfaces, *Advanced Materials Interfaces* **3**, 1600478 (2016), <https://onlinelibrary.wiley.com/doi/pdf/10.1002/admi.201600478>.
- [7] K. Kargupta and A. Sharma, Templating of thin films induced by dewetting on patterned surfaces, *Phys. Rev. Lett.* **86**, 4536 (2001).
- [8] J. Koplik, T. S. Lo, M. Rauscher, and S. Dietrich, Pearling instability of nanoscale fluid flow confined to a chemical channel, *Physics of Fluids* **18**, 032104 (2006), <https://doi.org/10.1063/1.2178786>.

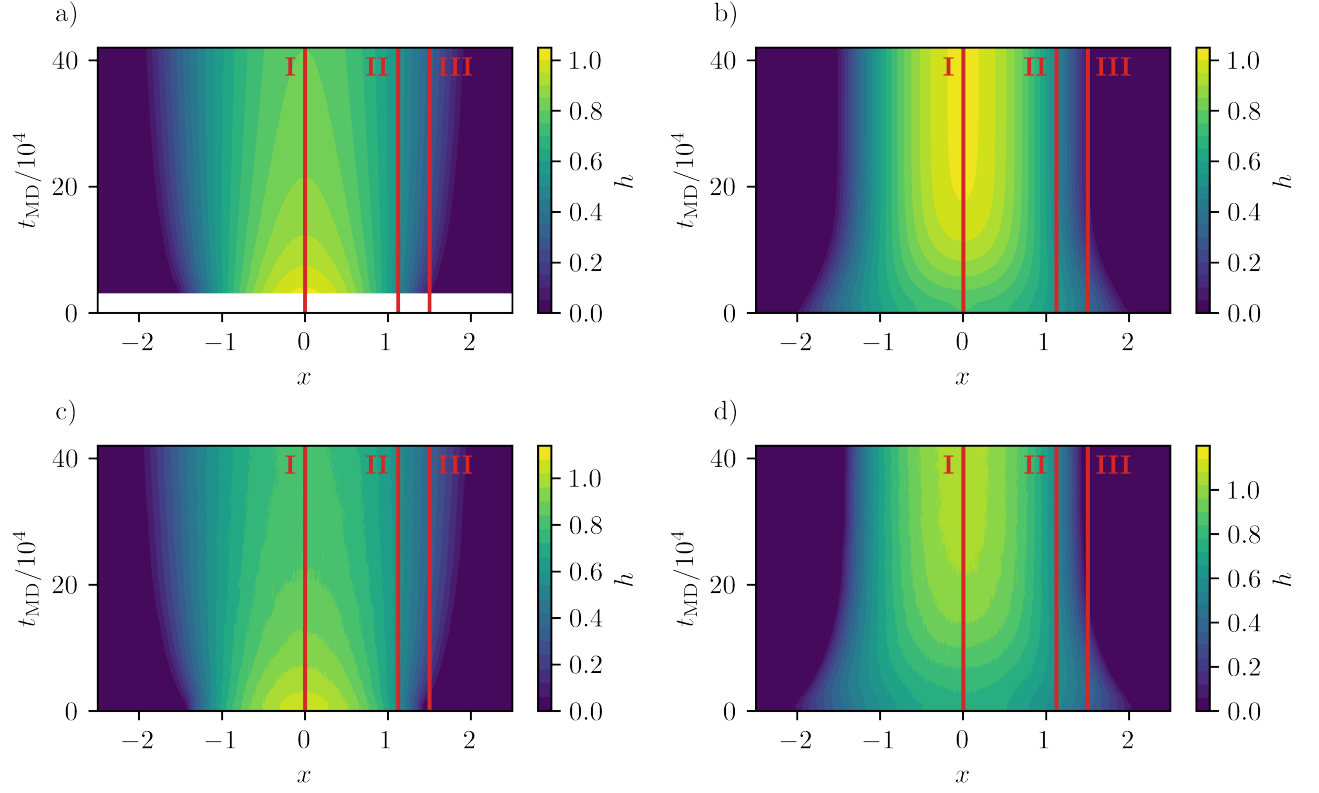


FIG. 17: Space-time plots showing the evolution of the height profile after a change in wettability for $\varepsilon_{\text{HW}} = 0.762$ and $\varepsilon_{\text{LW}} = 0.632$ for a temperature of $T = 0.70$. a) and c) switch from low to high wettability in the TFE and the MD model, respectively. b) and d) show inverse switching direction in the TFE and the MD model, respectively. Red vertical lines labeled I, II and III indicate at which positions the height profile evolution is shown in Fig. 18.

- [9] M. Wilczek, J. Zhu, L. Chi, U. Thiele, and S. V. Gurevich, Dip-coating with prestructured substrates: transfer of simple liquids and langmuir-blodgett monolayers, *J. Phys. Condens. Matter* **29**, 014002 (2016).
- [10] H. Wang, O. Buller, W. Wang, A. Heuer, D. Zhang, H. Fuchs, and L. Chi, Area confined position control of molecular aggregates, **18**, 053006 (2016).
- [11] C. Honisch, T.-S. Lin, A. Heuer, U. Thiele, and S. V. Gurevich, Instabilities of layers of deposited molecules on chemically stripe patterned substrates: Ridges versus drops, *Langmuir* **31**, 10618 (2015).
- [12] P. Lenz and R. Lipowsky, Morphological transitions of wetting layers on structured surfaces, *Phys. Rev. Lett.* **80**, 1920 (1998).

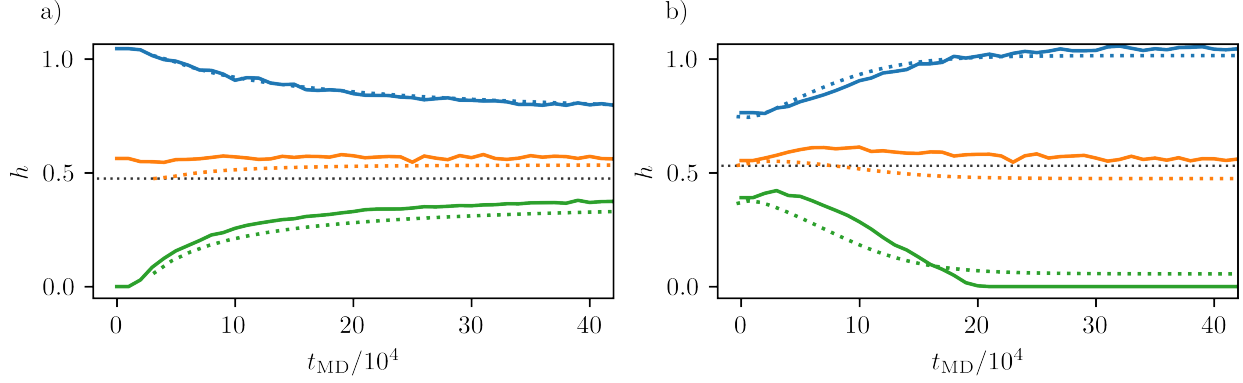


FIG. 18: Three characteristic height profiles along the marked lines I (blue), II (orange) and III (red) as shown in Figure 17. The height profiles extracted from the MD model are presented with solid lines. The dotted lines are TFE results with the temporal scaling obtained using our mapping approach. The height h is given relative to the maximum height. The black dotted line indicates the initial height in the TFE model for slice II to emphasize the non monotonous behavior for the height profile at this position. a) the wettability is switched from low to high, b) the wettability is switched in the opposite direction.

- [13] W. Tewes, O. Buller, A. Heuer, U. Thiele, and S. V. Gurevich, Comparing kinetic monte carlo and thin-film modeling of transversal instabilities of ridges on patterned substrates, *The Journal of Chemical Physics* **146**, 094704 (2017), <https://doi.org/10.1063/1.4977739>.
- [14] H. F. Wu, K. A. Fichthorn, and A. Borhan, An atomistic–continuum hybrid scheme for numerical simulation of droplet spreading on a solid surface, *Heat and Mass Transfer* **50**, 351 (2014).
- [15] J. Zhang, M. K. Borg, and J. M. Reese, Multiscale simulation of dynamic wetting, *International Journal of Heat and Mass Transfer* **115**, 886 (2017).
- [16] R. Wang, K. Hashimoto, A. Fujishima, M. Chikuni, E. Kojima, A. Kitamura, M. Shimohigoshi, and T. Watanabe, Light-induced amphiphilic surfaces, *Nature* **388**, 431 (1997).
- [17] X. Feng, J. Zhai, and L. Jiang, The fabrication and switchable superhydrophobicity of tio2 nanorod films, *Angewandte Chemie International Edition* **44**, 5115 (2005), <https://onlinelibrary.wiley.com/doi/pdf/10.1002/anie.200501337>.
- [18] R.-D. Sun, A. Nakajima, A. Fujishima, T. Watanabe, and K. Hashimoto, Photoinduced surface wettability conversion of zno and tio2 thin films, *The Journal of Physical Chemistry B* **105**, 1984 (2001).
- [19] K. Ishihara, A. Okazaki, N. Negishi, I. Shinohara, T. Okano, K. Kataoka, and Y. Sakurai, Photo-induced change in wettability and binding ability of azoaromatic polymers, *Journal of Applied Poly-*

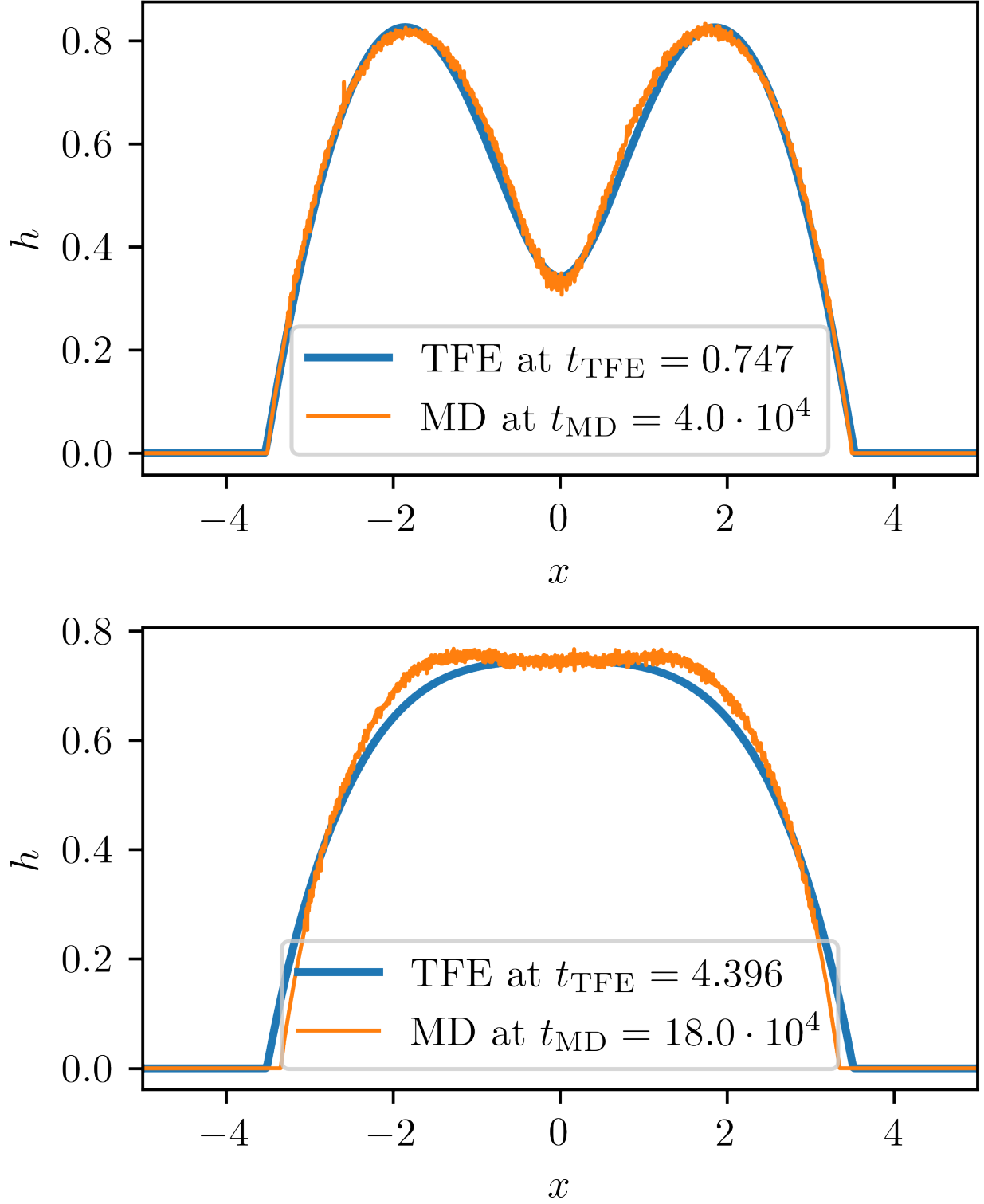


FIG. 19: Two examples of a height profile from MD simulations matched to a height profile from the TFE model taken from the coalescence simulation shown in Fig. 8.

- mer Science **27**, 239 (1982), <https://onlinelibrary.wiley.com/doi/pdf/10.1002/app.1982.070270125>.
- [20] R. Rosario, D. Gust, M. Hayes, F. Jahnke, J. Springer, and A. A. Garcia, Photon-modulated wettability changes on spiropyran-coated surfaces, *Langmuir* **18**, 8062 (2002), <https://doi.org/10.1021/la025963l>.
- [21] F. Zhu, S. Tan, M. K. Dhinakaran, J. Cheng, and H. Li, The light-driven macroscopic directional motion of a water droplet on an azobenzene-calix[4]arene modified surface, *Chem. Commun.* **56**, 10922 (2020).
- [22] W. Jiang, G. Wang, Y. He, X. Wang, Y. An, Y. Song, and L. Jiang, Photo-switched wettability on an electrostatic self-assembly azobenzene monolayer, *Chem. Commun.* , 3550 (2005).
- [23] J. Groten, C. Bunte, and J. Rühe, Light-induced switching of surfaces at wetting transitions through photoisomerization of polymer monolayers, *Langmuir* **28**, 15038 (2012), pMID: 22967018, <https://doi.org/10.1021/la302764k>.
- [24] K. Ichimura, S.-K. Oh, and M. Nakagawa, Light-driven motion of liquids on a photoresponsive surface, *Science* **288**, 1624 (2000), <https://science.sciencemag.org/content/288/5471/1624.full.pdf>.
- [25] J. Grawitter and H. Stark, Steering droplets on substrates using moving steps in wettability, *Soft Matter* **17**, 2454 (2021).
- [26] T. M. Squires and S. R. Quake, Microfluidics: Fluid physics at the nanoliter scale, *Rev. Mod. Phys.* **77**, 977 (2005).
- [27] M. P. Allen and D. J. Tildesley, *Computer Simulation of Liquids: Second Edition*, 2nd ed. (Oxford University Press, Oxford, 2017) p. 640.
- [28] M. J. de Ruijter, T. D. Blake, and J. De Coninck, Dynamic wetting studied by molecular modeling simulations of droplet spreading, *Langmuir* **15**, 7836 (1999), <https://doi.org/10.1021/la990171l>.
- [29] J. Roy Choudhuri and P. Nath, Wetting transition of a nanodrop on switchable hydrophilic-hydrophobic surfaces, *Surfaces and Interfaces* **21**, 100628 (2020).
- [30] A. Oron, S. H. Davis, and S. G. Bankoff, Long-scale evolution of thin liquid films, *Reviews of Modern Physics* **69**, 931 (1997).
- [31] D. Bonn, J. Eggers, J. Indekeu, J. Meunier, and E. Rolley, Wetting and spreading, *Reviews of Modern Physics* **81**, 739 (2009).
- [32] U. Thiele, Thin film evolution equations from (evaporating) dewetting liquid layers to epitaxial growth (2010).
- [33] N. G. Hadjiconstantinou, Combining atomistic and continuum simulations of contact-line motion, *Phys. Rev. E* **59**, 2475 (1999).

- [34] P. G. de Gennes, Wetting: statics and dynamics, *Rev. Mod. Phys.* **57**, 827 (1985).
- [35] A. P. Hughes, U. Thiele, and A. J. Archer, Influence of the fluid structure on the binding potential: Comparing liquid drop profiles from density functional theory with results from mesoscopic theory, *The Journal of Chemical Physics* **146**, 064705 (2017), <https://doi.org/10.1063/1.4974832>.
- [36] N. Tretyakov, M. Müller, D. Todorova, and U. Thiele, Parameter passing between molecular dynamics and continuum models for droplets on solid substrates: The static case, *The Journal of Chemical Physics* **138**, 064905 (2013).
- [37] A. P. Hughes, U. Thiele, and A. J. Archer, Liquid drops on a surface: Using density functional theory to calculate the binding potential and drop profiles and comparing with results from mesoscopic modelling, *The Journal of Chemical Physics* **142**, 074702 (2015), <https://doi.org/10.1063/1.4907732>.
- [38] O. Buller, W. Tewes, A. J. Archer, A. Heuer, U. Thiele, and S. V. Gurevich, Nudged elastic band calculation of the binding potential for liquids at interfaces, *The Journal of Chemical Physics* **147**, 024701 (2017), <https://doi.org/10.1063/1.4990702>.
- [39] J. A. Anderson, J. Glaser, and S. C. Glotzer, Hoomd-blue: A python package for high-performance molecular dynamics and hard particle monte carlo simulations, *Computational Materials Science* **173**, 109363 (2020).
- [40] P. J. Hoogerbrugge and J. M. V. A. Koelman, Simulating microscopic hydrodynamic phenomena with dissipative particle dynamics, *Europhysics Letters (EPL)* **19**, 155 (1992).
- [41] C. L. Phillips, J. A. Anderson, and S. C. Glotzer, Pseudo-random number generation for brownian dynamics and dissipative particle dynamics simulations on gpu devices, *Journal of Computational Physics* **230**, 7191 (2011).
- [42] T. Ingebrigtsen and S. Toxvaerd, Contact angles of lennard-jones liquids and droplets on planar surfaces, *The Journal of Physical Chemistry C* **111**, 8518 (2007), <https://doi.org/10.1021/jp0676235>.
- [43] J. H. Weijs, A. Marchand, B. Andreotti, D. Lohse, and J. H. Snoeijer, Origin of line tension for a lennard-jones nanodroplet, *Physics of Fluids* **23**, 022001 (2011), <https://doi.org/10.1063/1.3546008>.
- [44] M. Kanduč, Going beyond the standard line tension: Size-dependent contact angles of water nanodroplets, *The Journal of Chemical Physics* **147**, 174701 (2017), <https://doi.org/10.1063/1.4990741>.
- [45] V. S. Mitlin, Dewetting of solid surface: Analogy with spinodal decomposition, *Journal of Colloid and Interface Science* **156**, 491 (1993).
- [46] R. Fetzer, K. Jacobs, A. Münch, B. Wagner, and T. P. Witelski, New slip regimes and the shape of dewetting thin liquid films, *Phys. Rev. Lett.* **95**, 127801 (2005).

- [47] S. Engelnkemper, *Nichtlineare Analyse physikochemisch getriebener Entnetzung - Statik und Dynamik*, Ph.D. thesis, Westfälische Wilhelms-Universität Münster (2017).
- [48] M. Heil and A. L. Hazel, oomph-lib – an object-oriented multi-physics finite-element library, in *Fluid-Structure Interaction*, edited by H.-J. Bungartz and M. Schäfer (Springer Berlin Heidelberg, Berlin, Heidelberg, 2006) pp. 19–49.
- [49] D. E. Sullivan, Surface tension and contact angle of a liquid–solid interface, *The Journal of Chemical Physics* **74**, 2604 (1981), <https://doi.org/10.1063/1.441333>.
- [50] R. Pandit, M. Schick, and M. Wortis, Systematics of multilayer adsorption phenomena on attractive substrates, *Phys. Rev. B* **26**, 5112 (1982).
- [51] E. H. Hauge and M. Schick, Continuous and first-order wetting transition from the van der waals theory of fluids, *Phys. Rev. B* **27**, 4288 (1983).
- [52] S. Dietrich and M. Schick, Critical wetting of surfaces in systems with long-range forces, *Phys. Rev. B* **31**, 4718 (1985).
- [53] S. Dietrich and M. Schick, Order of wetting transitions, *Phys. Rev. B* **33**, 4952 (1986).
- [54] N. Kubochkin and T. Gambaryan-Roisman, Wetting at nanoscale: Effect of surface forces and droplet size, *Phys. Rev. Fluids* **6**, 093603 (2021).
- [55] A. Münch, B. Wagner, and T. P. Witelski, Lubrication models with small to large slip lengths, *Journal of Engineering Mathematics* **53**, 359 (2005).
- [56] U. Thiele, Recent advances in and future challenges for mesoscopic hydrodynamic modelling of complex wetting, *Colloids and Surfaces A: Physicochemical and Engineering Aspects* **553**, 487 (2018).
- [57] B. Wyart and P. de Gennes, Dynamics of partial wetting, *Advances in Colloid and Interface Science* **39**, 1 (1992).
- [58] M. M. Iler and L. G. Iez MacDowell, Wetting of polymer liquids: Monte carlo simulations and self-consistent field calculations, *Journal of Physics: Condensed Matter* **15**, R609 (2003).
- [59] V. P. Carey and A. P. Wemhoff, Disjoining Pressure Effects in Ultra-Thin Liquid Films in Micropassages—Comparison of Thermodynamic Theory With Predictions of Molecular Dynamics Simulations, *Journal of Heat Transfer* **128**, 1276 (2006), https://asmedigitalcollection.asme.org/heattransfer/article-pdf/128/12/1276/5914906/1276_1.pdf.
- [60] L. MacDowell, Computer simulation of interface potentials: Towards a first principle description of complex interfaces?, *The European Physical Journal Special Topics* **197**, 131 (2011).

- [61] D. N. Sibley, P. Llombart, E. G. Noya, A. J. Archer, and L. G. MacDowell, How ice grows from premelting films and water droplets, *Nature communications* **12**, 1 (2021).
- [62] M. Stieneker, L. Topp, S. Gurevich, and A. Heuer, Data supplement for 'multiscale perspective on wetting on switchable substrates: mapping between microscopic and mesoscopic models' 10.5281/zenodo.5723440 (2021).
- [63] S. Seabold and J. Perktold, statsmodels: Econometric and statistical modeling with python, in *9th Python in Science Conference* (2010).